INSTITUTO
UNIVERSITÁRIO
DE LISBOA

Laser phase noise impaired next generation short-reach networks employing MCFs and Kramers Kronig receivers

Filipe Martins Saraiva

Master Telecommunications and Computer Engineering

Supervisor:
Ph.D Tiago Manuel Ferreira Alves, Assistant Professor
Iscte - Instituto Universitário de Lisboa

November 2022

Laser phase noise impaired next generation short-reach networks employing MCFs and Kramers Kronig receivers

Filipe Martins Saraiva

Master Telecommunications and Computer Engineering

Supervisor:
Ph.D Tiago Manuel Ferreira Alves, Assistant Professor
Iscte - Instituto Universitário de Lisboa

November 2022

Acknowledgment

I would like to express my gratitude to my supervisor, Prof. Dr. Tiago Manuel Ferreira Alves for all the guidance and support during this project, without him this work would not be possible. I would also like to acknowledge the research scholarship provided by Instituto de Telecomunicações.

Abstract

In this work, a short-reach network employing multicore fibers (MCF) and Kramers Kroning (KK) receivers is proposed. The impact of the combined effect of the laser phase noise and the intercore crosstalk (ICXT) on the performance of the proposed system is assessed.

It is shown that the impact of the laser phase noise depends on the product between the skew and the laser linewidth (|linewidth×skew|). Thus, the performance of the proposed short-reach MCF-based systems has been assessed considering |linewidth×skew| << 1. Studies for systems with the product between the skew and the symbol rate much higher than one (|skew×Rs| >>1) and much lower than one (|skew×Rs| <<1) are accomplished. It is shown that between the case |skew×Rs| <<1 and |skew×Rs| >>1, there is a reduction in STAXT variances of 10%. When |linewidth×skew| << 1, for different values of laser linewidth, the value of the STAXT variance remains constant, but for |linewidth×skew| >> 1 there is a decrease in STAXT variance of 90% for higher|skew×Rs|. It is suggested that systems with |skew×Rs| <<1 are more dependent on the optical source linewidth of the interfered core. It is also shown that for |skew×Rs| <<1 considering a 10 MHz on both cores, an additional margin of 10 dB of ICXT may be needed relative to an ideal laser to obtain the same outage probability. It is suggested that this degradation is manly caused by the laser phase noise in the interfered core.

Keywords: Laser phase noise; short-reach networks; multicore fiber; Kramers Kronig receivers

Resumo

Neste trabalho é proposta uma rede de curto alcance que utiliza fibras multi núcleo (MCF) e receptores Kramers Kroning (KK). O impacto do efeito combinado do ruído de fase do laser e do intercore crosstalk (ICXT) no desempenho do sistema proposto é avaliado.

Foi demonstrado que o impacto do ruído de fase do laser depende do produto entre o skew e a largura da linha do laser (|linewidth×skew|). Assim, o desempenho dos sistemas baseados em MCF de curto alcance propostos foi avaliado considerando |linewidth×skew| << 1. Estudos para sistemas com o produto entre o skew e o ritmo de símbolo muito maior que um (|skew×Rs| >>1) e muito menor que um (|skew×Rs| <<1) são realizados. Mostra-se para o sistema estudado que entre o caso |skew×Rs| <<1 e |skew×Rs| >>1, há uma redução na variância STAXT de 10%. Quando |linewidth×skew| << 1 o valor da variância STAXT permanece constante, mas para |linewidth×skew| >> 1 existe uma diminuição na variância STAXT de 90% para |skew×Rs| maiores. É sugerido ainda que os sistemas com |skew×Rs| <<1 sejam mais dependentes da fonte óptica do nucleo interferido. Também é demostrado que para |skew×Rs| <<1 considerando 10 MHz em ambos os núcleos, uma margem adicional de 10 dB de ICXT pode ser necessária em relação a um laser ideal para obter a mesma probabilidade de interrupção. É sugerido que esta degradação é causada principalmente pelo ruído de fase presente no núcleo interferido.

Palavras-chave: Ruído de fase do laser; redes de curto alcance; fibras multi núcleo; receptores Kramers Kronig.

Contents

List of Figures

List of Tables

List of Acronyms

BER Bit error rate

CD Chromatic Dispersion
CSPR Carrier to Signal Power Ratio
CW Continuous Wave
CWDM Coarse Wavelength Division Multiplexing

DAC Digital to Analog
DCF Dispersion Compensation Fiber
DCM Discrete Changes Model
DD Direct Detection
DFB Distributed Feedback Lasers
DP-MZM Dual Parallel Mach-Zehnder Modulator
DSP Digital Signal Processing
DWDM Dense Wavelength Division Multiplexing

ECL External Cavity Lasers
EDFA Erbium-Doped Fiber Amplifier
EVM Error Vector Magnitude

FEC Forward Error Correction
FMF Few-mode Fiber

ICP Internet Content Providers
ICXT Inter-core Crosstalk

KK Kramers-Kronig
KK-PAM Pulse Amplitude Modulation KK

LO Local Oscillator

MCF Multicore Fiber
MMF Multimode Fiber
MZM Mach-Zehnder Modulator

NEP Noise Equivalent Power

OP Outage Probability
OSNR Optical Signal-to-noise Ratio

P2A Phase To Amplitude

PAM Pulse Amplitude Modulation
PAPR Peak-to-average Power Ratio
PD Photodiode
PDF Probability Distribution Function
PSD Power Spectral Density

QAM Quadrature Amplitude Modulation

RC Raised Cosine
RRC Root-raised Cosine

SC-MCF Strongly-Coupled Multicore Fiber
SDM Space Division Multiplexing
SMF Single Mode Fiber
SSBI Signal-to-signal Beat Interference
STAXT Short-Term Average Crosstalk

TS-KK Two-Sided KK Receiver

WC-MCF Weakly-Coupled Multicore Fiber
WDM Wavelength Division Multiplexing

List of Symbols

α Fibre attenuation
β Roll-off factor
β_0 Propagation constant
β_1 Propagation time delay
β_2 Group velocity dispersion
β_3 High order dispersion
$\boldsymbol{H}$ Hilbert transform
$\Delta\overline{\beta}_{mn}(\omega)$ Difference between the averages of the propagation constants of both cores
$\Delta\upsilon_l$ Laser linewidth
λ_0 Operating wavelength
$\mathfrak{F}^{-1}$ Inverse Fourier transform
ω Angular frequency
$\overline{K}_{nm}$ Average inter-core coupling coefficient
$\phi(t)$ Laser phase noise
$\phi_{p,b}^{(k)}$ RPS of the k-th PMP
erfc(x) Complementary error function of x
ln(x) Natural logarithm of x
max(x) Maximum value of x
$\varphi(t)$ Information signal phase
A Amplitude of the optical carrier
B Spectral shift applied to the signal
c Speed of light in vacuum
D_{λ_0} Dispersion parameter
$E(t)$ Complex optical field of the signal
e_1 Field at the output of the upper arm of the DP-MZM
e_2 Field at the output of the lower arm of the DP-MZM
$E_{ICXT}(t)$ Optical ICXT field at the output of the test core
$E_{in,1}$ Optical field at the input of the DP-MZM upper arm
$E_{in,2}$ Optical field at the input of the DP-MZM lower arm
E_{in} Optical field at DP-MZM input
$E_{m,x}(t)$ Polarization x of the optical signal launched to the input of the interfering core
$E_{m,y}(t)$ Polarization y of the optical signal launched to the input of the interfering core
$E_{n,x}(t)$ Polarization x of the optical signal launched to the input of the interfered core
$E_{n,y}(t)$ Polarization y of the optical signal launched to the input of the interfered core
e_{out} Optical field at the output of the DP-MZM
$F_{p,b}$ ICXT transfer function
$H(f)$ SSMF transfer function
$H_{rc}(f)$ RC filter transfer function

$H_{rrc}(f)$ RRC filter transfer function
$i(t)$ Electric current after photodetection
L Fibre length
$n(\tau)$ White Gaussian noise
n_{eff} Refractive index of the core
P_m Power at the output of the interfering core
P_n Power at the output of the interfered core
$p_{icxt}(t)$ Instantaneous ICXT power
R_λ PIN responsivity
$S(t)$ Information signal
S_{λ_0} Slope of the dispersion parameter
$STAXT_n(t)$ Average ICXT power measured during a short period
T_s Symbol period
V_1 Electrical signal applied to upper arm
V_2 Electrical signal applied to lower arm
$v_i(t)$ In-phase component of the signal
$v_q(t)$ Quadrature component of the signal
$V_{b,1}$ Upper arm bias voltage of DP-MZM
$V_{b,2}$ Lower arm bias voltage of DP-MZM
$V_{b,3}$ Bias voltage of the outer DP-MZM
V_{sv} Switching voltage of the MZM
X_c ICXT level
z_k Longitudinal coordinate of the k-th PMP

Chapter 1
Introduction

1.1. Motivation

In recent years, the need for short-range, high capacity and low-cost connections has been increasing. In response to this need, two technologies were proposed: multicore fibers (MCF) and Kramers-Kronig (KK) receivers. While multicore fibers increase the density of connections [**1**], KK receivers allow to use direct-detection with a single photodiode, enabling lower consumption, signal linearization and maintaining high bit rates at low cost [**2**].

In order to obtain a functional low-cost system, it is necessary to use also off-the-shelf lasers. However the use of low cost lasers present some disadvantages associated with large laser linewidth and higher phase noise variance. This, in the presence of dispersion is converted to amplitude noise and may affect the linearization of the KK receiver and impairs the system performance [**3**].

1.2. Context

Currently, optical fiber networks are reaching the so-called capacity crunch of 100 Tb/s per single core fiber [**4**]. Space division multiplexing (SDM) is a powerful solution to increase the system capacity, since this technology exploits the only physical dimension left to be used in optical networks, the spatial dimension. Using multicore fibres, a type of SDM, it is theoretically possible to increase the capacity of the optical network N times over the current single-mode fibre networks, N being the number of cores within a fibre. This technology has been proposed to solve the following problems:

(1) the growing capacity demands in core networks, through new advanced transmission techniques and/or modulation formats. [**5**]
(2) the space limitations in short-reach networks as intra or inter data-center communications. [**1**]

Duo to cost purposes, MCF short-reach networks need to employ a low cost laser source at the transmitter side and direct detection (DD) in the receiver. However the usage of low cost laser may introduce large phase noise variance and DD receivers will impair the connection by introducing signal-to-signal beating interference (SSBI). In this work, the KK receiver is proposed for receiver linearization in >200 Gb/s MCF short-reach networks and the impact of the laser phase noise on the performance is assessed.

1.3. Goals

The general purpose of this work is to unlock the capacity supported by next generation optical networks. This is accomplished by proposing an SDM short-reach network for

data center interconnects with a dedicated capacity per user of >200 Gb/s and using low-cost lasers with DSP-based direct-detection receivers employing KK technique for receiver linearization. Particularly, the following objectives are pursued:

(1) To integrate a software platform for simulation of short-reach >200 Gb/s SDM optical fibre networks employing real laser sources and the KK receiver;
(2) To identify the main operational issues of the proposed short-reach SDM network;
(3) To assess the impact of the combined effect of the laser phase noise and random nature of the inter-core crosstalk (ICXT) along time on the performance of the proposed short-reach network employing KK receivers.

1.4. Methodology

The general activity of this work is to develop a short-reach SDM network simulator with >200 Gb/s per optical channel employing low-cost laser sources and KK technique for receiver linearization and to assess the performance dependence of these networks on the laser phase noise when the ideal implementation of the KK technique is employed. This is accomplished by performing the following tasks:

(1) To develop a Matlab software that generates and detects a 200 Gb/s optical signal;
(2) To include the laser phase noise modelling on the simulator;
(3) To identify and implement the ideal implementation of the KK technique;
(4) To include the MCF propagation in the simulator;
(5) To develop simulations in order to specify the reach, capacity and laser requirements for these short-reach MCF networks;
(6) To evaluate the impact of the combined effect of the ICXT and laser phase noise has on the system outage probability.

1.5. Structure of the dissertation

This dissertation will be organize as followed:

Chapter 2 presents the review of the literature used in this work. It describes the main challenges and the requirements of current data centers, discusses SDM technology and KK receivers as potential solutions to increase capacity in data centers. This chapter also contains the analysis of the phase noise and the problem of employing low cost lasers.

Chapter 3 describes the system used in the simulation. Each component of the system is introduced and simulation models are described. Metrics used to evaluate the system performance are also introduced .

Chapter 4 presents the results for the different simulations done. The impact of the combined effect of the laser phase noise and the ICXT on the short-term average crosstalk (STAXT), system bit-error rate (BER) and outage probability are assessed.

Chapter 5 presents the final conclusion and suggests some future work.

1.6. Main original contributions

The main contributions of this work are:

- To evaluate the combined effect of the ICXT and laser phase noise on a system employing a KK receiver and multicore fibers.
- To assess the outage probability of a MCF-based system employing KK receivers and off-the-shelf lasers impaired by laser phase noise.

Chapter 2
Literature Review

This chapter summarizes the state-of-the art of the main topics addressed in this work. It focuses on current optical networks, the problems and their limits. This chapter also discusses the requirements and challenges of data centers and provides a summary of the proposed solutions based on MCF and KK receivers.

2.1. Data-centers

With the traffic increasing at a rate of 31.9% from data center to data center [**6**], traditional data center structures (with 3 tiers) will not be the most suitable for the near future. Currently, internet content providers (ICP) need to process a very large amount of information, due to cloud computing for example [**5**], making architecture that manage traffic "north-south" (traffic that is outside data centers to servers) less optimal. This need to process a large amount of information has made paradigm shift in the architecture of data centers from the traditional structure to an east-west traffic structure [**5**]. This is a more convenient structure for the management of traffic that goes from one server to another server facilitating the interconnectivity between data centers in the vicinity (less than 100 km) [**5**].

Using east-west traffic structure with 2 tiers will increases the number of links between data centers, therefore increasing the number of intra and inter data center connections. The increasing number of intra and inter data center connections will increase the demand for their capacity while wanting to keep an overall low cost.

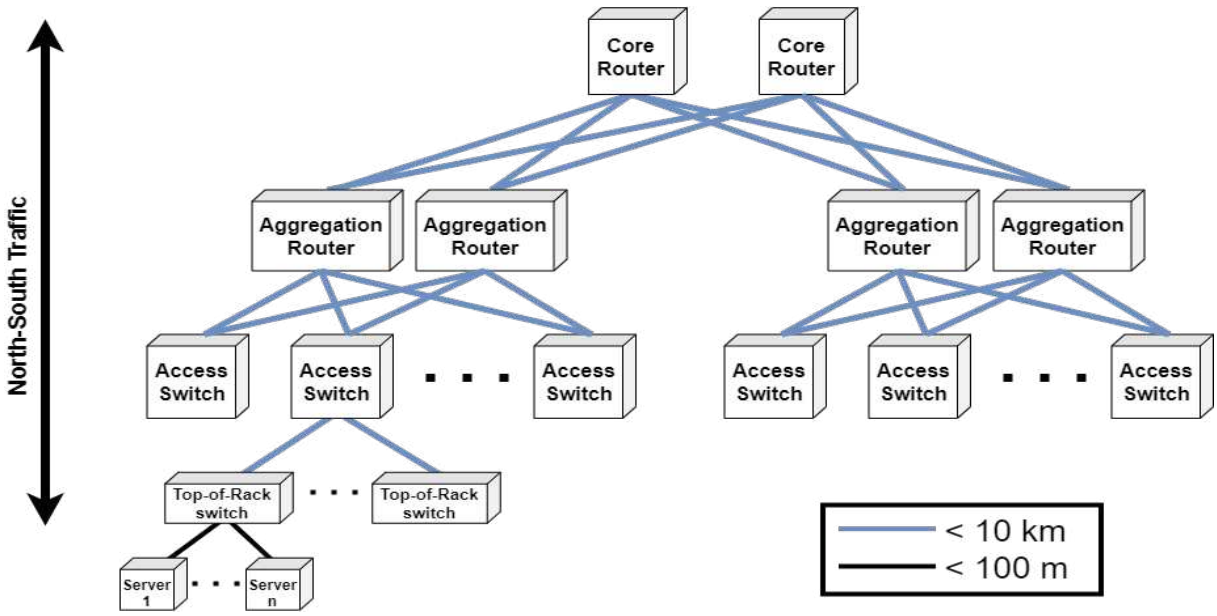

FIGURE 1. Traditional three-tier data center architecture.

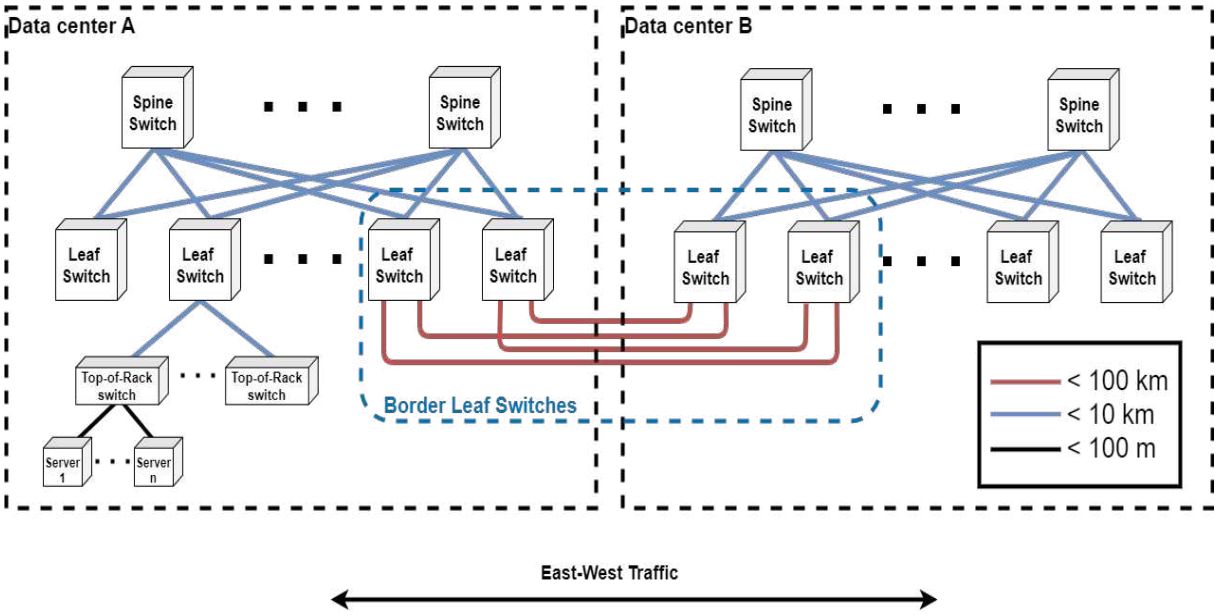

FIGURE 2. New two-tier data center architecture.

Figure 1 depictes the traditional three tier data center architecture. The traffic goes from the core routers to the server bellow (north-south) making it useful for getting the traffic outside the data center to the servers bellow but not for connecting two different data centers. This type of architecture thereby relays more on intra data centers connections. Figure 2, the new data center architecture with two tiers is shown. This type of architecture allows a much better connectivity between data centers with the border leaf switches that allow the connection between different data centers. Expanding this type of data center is also much more manageable with the only requirement being adding more leaf switches or spine switches as needed [**5**]. This connections (depicted in red in figure 2) are usually less than 100 km and represent the inter data center connections treated in this dissertation.

2.1.1. Data-centers requirements

Current intra-data center connections (less than 10km of range) use wavelengths in the second window (1310 nm). In this wavelengths the chromatic dispersion is reduced. Thus, in short distances there is no need for chromatic dispersion compensation, reducing the overall cost for each short-haul connection [**5**]. For multiplexing, it use mainly coarse wavelength division multiplexing (CWDM), with a channel spacing of 20 nm or to avoid power-hungry laser temperature control [**5**]. As the distances are short it is not necessary amplification. Overall making the cost of the connection as low as possible.

For the inter-data center connections (less than 100km) line amplification is a requirement and, for this purpose EDFAs are used [**5**]. As EDFAs have the limitation of working only in the third window, it is necessary to use wavelengths in range of 1550 nm. With longer distances and higher wavelengths, it will also be necessary to compensate the chromatic dispersion. For this purpose, several options, like electronic compensation

or an option that is less power-hungry, Dispersion compensation fibers (DCFs) have been proposed [**5**].

2.1.2. Solutions for new data centers

In today's data centers, the most used technology for multiplexing is the wavelength division multiplexing (WDM) complemented with the use of multiple fiber cables [**5**]. But this strategy is not scalable and show higher cost and complexity for higher bit rates because more power and more fibers will be needed.

To answer these problems SDM is one of the suggested technologies [**7**]. When implemented for short-haul connection it will not only allow a huge increase in the number of transmission channels but will also reduce the fiber density within the data-center solving two problems for short-haul connections [**1**]. This subject will be dealt with in the following section.

To increase the system performance without the high costs of coherent detection systems the use of KK receiver with low cost lasers is being studied [**2**]. The KK receivers enables a more advanced direct detection. By guaranteeing the minimum phase condition [**8**], with just the intensity measurement it is also possible to recover the phase of the signal as well. This makes it possible to increase system performance without increasing cost. The KK receiver will also allow the usage of digital compensation of the signal while using direct detection. This type of receiver will be treated in the section 2.3.

2.2. Space division multiplexing

Data centers usually rely on single mode fiber (SMF) to establish connections. However, with SMF, the capacity may not pass the 100 Tb/s limit [**7**]. One solution to overcome the optical system limit imposed by Shannon information theory is SDM. This technology exploits the last know physical propriety of the fiber (space) allowing it to reach more capacity in the next years. There are currently three main approaches being studied to fully utilize SDM: multiple fibers, multicore fiber (MCF) and few-modes fiber (FMF) [**7**]. Over the last few years a lot of research has been done on the SDM. Solutions for long-haul connections have been shown in [**9**–**11**] and solutions for short-haul have been shown in [**12**–**14**]. These studies show the viability to use SDM not only of long-haul but also for inter-data center connections.

2.2.1. Multiple fibers

While usually SDM is associated with MCF on FMF, the simple and oldest case of SDM is employing multiple fibers in a single cable [**15**]. This type of SDM is simple to use as it does not need any new technology. However, for data center with limited space the system scalability by employing multiple fibers may be impairing.

2.2.2. Few-modes fiber

Few-mode fiber is a type of multimode fiber (MMF). Multimode fiber is similar to a SMF, however, it has a bigger core allowing it to have multiple modes to propagate

information. The problem with MMF is that it has a strong and often uncontrollable intermodal coupling that is usually a source of noise at the receiver [**16**]. With FMF, the target is to use few specific modes to propagate data signals inside a single core. Those modes are selected in a way so that interference between them is minimal, thus minimizing possible crosstalk [**16**].

2.2.3. Multicore fiber

In SDM technology, MCF is the one receiving more attention of the scientific community over the last years [**15**]. The MCF has low complexity and demonstrates that it is possible to reach a large number of channels without compromising the system viability. The main idea of MCF is to incorporate many cores inside a single fiber while trying to manage the crosstalk between adjacent cores [**7**]. Multicore fibers have been proposed in recent years as potential solution to increase capacity not only in short-reach [**1**] systems, but also in long-haul connections [**7**].

Within the MCFs, there are two major categories: the weakly-coupled MCF (WC-MCF) and the strongly-coupled MCF (SC-MCF) [**7**]. The main difference between both fiber types is the distance between the cores. Strongly-coupled MCF have cores much closer which allows the fiber to have more cores, which enables more channels for information transmission. However, since the cores are closer to each other the crosstalk between cores will be higher. As increasing the diameter of the fibers cladding is not a viable solution because the fiber need to maintain high mechanical reliability for bending [**7**], to decrease the crosstalk between cores, we have to decrease the distance between the cores. In weakly-coupled MCF, the cores are separated by a greater distance, which limits the core density, but allows a much more manageable crosstalk between cores.

MCF can also be grouped in homogeneous and heterogeneous MCF. If the cores inside the MCF have the same refractive indexes then they are homogeneous MCFs. When the cores inside the MCF have different refractive indexes then it is a heterogeneous MCF.

2.2.4. Advantages and disadvantages of MCF

The most obvious advantage of MCFs is the ability to use different cores as independent channels to transmit different signals. Taking into account that this technology is compatible with WDM, it is possible to increase the number of channels in a drastic way using MCFs, as proven in [**17**, **18**]. Another advantage that MCFs brings is the fact that they can reduce the density of connections in data centers [**1**]. As a fiber in theory can have more cores, not so many fibers will be needed for the same capacity and, theoretically, its possible to densely integrate multiple space channels into a single laser that will somewhat reduce the cost of the network [**1**].

One great disadvantage of MCF technology is the complexity when compared with SMF because we have to modify and adapt devices such as connectors for this new type of fiber, as shown in [**1**]. Another disadvantage is the worst performance caused by the inter-core crosstalk (ICXT), as in SMF only one core is used there is no crosstalk between

cores. The ICXT is a random process that have power variations which can lead signal-to-noise ratio (OSNR) degradation [**19**]. However there are techniques that allow the mitigation of the ICXT [**7**]. These techniques not only allow better performance for MCF in general but also allow the WC-MCF to have more cores without impairing the system performance [**7**].

2.2.5. What has been achieved and limitations

In this section, recent studies performed with MCF are analysed. As mentioned before, ICXT is one of the greatest limitations of MCFs and it depends on several variables, such as core refractive index and bending radius. There are already several techniques for estimating ICXT as demonstrated in [**7**]. These techniques are fundamental to be able to reduce the ICXT to levels where the MCFs can be used without great penalties.

New connectors to be used in MCF-based short-reach systems has been also investigated [**20**].With these connectors, the worst core has losses below 0.5 dB. It is also concluded that, although connectors for MCF are more challenging to employ, because of the need for a perfect alignment of all cores, results are similar to stantndard SMF connector.

The impact of MCF based system impaired by the laser phase noise has been adressed in [**21**]. It is shown that for large periods of time the combined affect of the ICXT and the laser phase noise can cause fluctuation in the throughput that exceed 2 Gb/s.

In [**22**], an analysis of the outage probability due do ICXT from multiple cores is presented. It is shown that the maximum of ICXT level accepted grows with core count, and it also depends on the skew bit rate product.

2.3. The Kramers-Kronig receiver

Optical fibre communications systems use two main types of receivers: direct detection (DD) based receivers and coherent detection base receivers. DD Receivers are the simplest, usually only requiring a single photo detector that measure the intensity of the optic field. Coherent receivers are more complex, usually requiring 4 photodetectors, a local oscillator, an hybrid coupler and complex digital signal processor (DSP) techniques for frequency offset, phase and dispersion compensation. This, in practices mean a better capacity in the system, since coherent detection is able to use of polarization diversity and both in-phase and quadrature components independently, allowing higher level modulations such quadrature amplitude modulation (QAM). However, this capacity improvement requires a much higher cost and for a data center with high number of connections this is not ideal. For this reason, in short-reach networks, to have a low cost connection, DD is preferable. To achieve the results of coherent detection with only direct detection, a more advance type of direct detection is proposed in [**8**].

The Kramers–Kronig receiver is one proposed solutions to achieve short distance connections with high bit-rate at low cost. This type of receivers uses the Kramers–Kronig relation [**8**], a well known set of equations already applied in different areas of physics. In

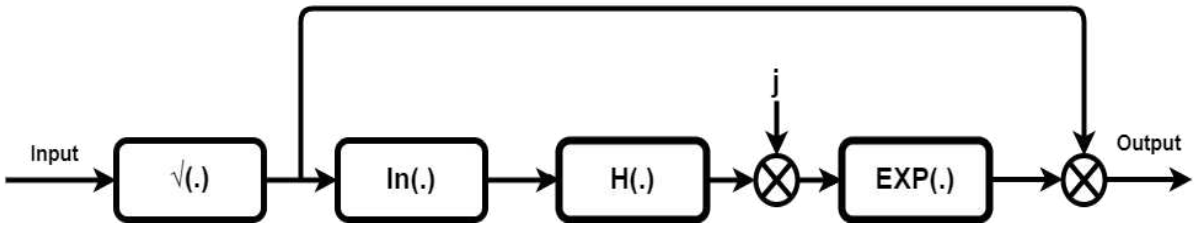

FIGURE 3. KK receiver block diagram

optics, this relation allows the reconstruction of the transmitted complex signal only with the measurement of its intensity. This can be achieved if the signal verifies the "minimum phase" condition. This condition is guaranteed if the carrier power is strong enough in relation to the signal [**8**]. With this relation it is possible to obtain both the in-phase and quadrature components of the signal with direct detection. Figure 3 show how this receiver can be implemented in as an optical receiver. This is a advantageous in relation to its coherent detection counterpart, as it not only requires less power consumption but also reduces the quantity of photo detectors and equipment cost. Another advantage of the KK receiver is the signal-to-signal beat interference (SSBI) cancellation [**23**]. The SSBI is generated by the nonlinearity at the photodiode (PD) [**24**], and if suppressed ,the receiver can be linearized.

The main disadvantages of this receiver is the need for a continuous wave (CW), this will imply that a notable fraction of the launched power need to be allocated to the CW [**8**]. This power does not carry any information and its only usage is to reconstruct the original complex signal.

2.3.1. Recent studies and limitations

In the last years, some studies have been done to test the performance of the KK receivers in short-reach systems.

Ref.	Bit-rate achieved per channel [Gb/s]	Distance [km]
[**25**]	data (line) rate: 182 (240)	100
[**26**]	data (line) rate: 182 (220)	125
[**27**]	80	160

TABLE 1. Bit rates achieved in systems employing Kramers-Kronig receivers.

Table 1 summarizes some some studies on short-reach systems employing KK receivers.

In [**25**], two differnt KK based receivers were used on a short-reach system. It was shown a 220 Gb/s single photodiode detection and a 4 channel 240 Gb/s dual polarization (dual photodiode) detection in a WDM system at 5.3 bits/s/Hz spectral efficiency. In [**26**], is shown a single laser, single polarization, single photodetector connetion with a line rate of 218 Gb/s. Employing QPSK and 16-QAM signals and using a CSPR of 7.5 dB the BER was bellow the FEC threshold. In [**27**], an 80 Gb/s 160 km QPSK signal was evaluated.

The impact of the chromatic dispersion in the KK receiver is shown. It is concluded that the KK receiver is sensitive to the CD since it can cause the minimum phase condition to be violated even for short distances. In [**28**], a 909.5 Tbit/s net data rate was achived by using MCF and WDM. In [**29**], a connection using the KK receiver and MCF it was shown that tera-bit-per-second data rates are achievable per WDM channel with one EDFA per fiber core. It was also shown that the employment of this technique has improved the space utilization in the data center and will potentially enable scalability and reconfigurability of the system architecture [**29**]. In [**30**], is shown the continuation of [**29**] and it was shown that the KK receiver significantly outperforms its IM/DD counterpart.

2.3.2. Types of Kramers-Kronig receivers

The KK relation has been used to develop different receivers as shown in [**25**, **31**]. These receivers have their advantages and disadvantages. For instance, the pulse amplitude modulation KK (KK-PAM) described in [**32**], is able to use pulse amplitude modulation (PAM) signal and it enables the compensation of CD digitally, making it ideal for low cost, short-reach connections. The only drawback is the requirement of a relatively expensive I/Q modulator [**31**]. Another example of a receiver based in the KK relation is the two-sided KK receiver (TS-KK). As stated in [**31**], the TS-KK as the advantage of accommodating polarization multiplexing. It also has the advantage of only using a local oscillator (LO) at the receiver. This allows the signal to be transmitted without the CW which would be responsible for power inefficiency. Its performance are similar to that of typical coherent receivers. However, it uses more bandwidth, since it has to guarantee a guard-band to separate the two side bands at the receiver, make it less spectral efficient.

2.4. Laser phase noise

When the laser is ideal and without any modulation, the power spectrum would only be composed by a single frequency centered at the oscillation frequency. Although optical sources are usually done through stimulated emission, in real cases, there is some amount of spontaneous emission. This will cause phase fluctuation in the laser. Due to this fluctuation, the laser can not be characterized by a single frequency in its power spectrum when no modulation is employed. Therefore, the optical source has some noise and it is not monochromatic, meaning that the power spectrum is characterized by spectral linewidth [**33**]. This linewidth usually characterizes the purity of the laser, meaning that lower linewidth implies a more pure but usually more expensive laser [**33**].

Usually two different types of laser are used. Distributed feedback Lasers (DFB) and external cavity lasers (ECL). DFBs have a linewidth of a few MHz while ECLs have a linewidth of a few kHz, making the ECL laser more pure but also more expensive. The phase noise generated by the laser imperfections, in DD systems, can affect signal power and also prevent the system from being linearized in the presence of chromatic dispersion [**2**]. Thus making it more difficult to make the digital compensation of the

signal with DSP. So without ensuring the linearization of the system it is difficult to ensure its detection without penalties.

2.4.1. Phase noise in Kramers-Kronig receivers

The presence of the phase noise in Kramers-Kronig receivers is still under research [**2**], since the laser phase noise can interact both with the carrier and the chromatic dispersion. When interacting with the carrier, this may have impact on the minimum phase condition as the phase noise may affect the carrier and the signal.

In [**24**], the KK receiver was employed to a short-reach network and it is taken into account the laser phase noise. In [**24**] the laser linewidth was varied between 0 and 6 MHz, and the SNR was assessed. It was concluded that when the laser linewidth was above 1.4 MHz and 2.5 MHz the phase noise become dominate. And for that reason maybe a challenge to employ lasers like distributed feedback Lasers (DFB).

In [**34**], a 64 QAM transmission over 480 km was performed. It was concluded that using a low cost laser like the distributed feedback laser (DFB) is viable but it is going to have a significant impact on the system performance.

In [**35**], the impact of the combined effect of laser phase noise and ICXT are evaluated in a DD-OOK based system employing MCF. It is also shown that the for systems with |linewidth×skew| $<<1$ the instantaneous ICXT power is independent of the laser phase noise. For systems with |linewidth×skew| $>>1$ as the contributions of the ICXT along the MCF at the interfered core output are uncorrelated due to the phase noise, the phase noise will impact the instantaneous ICXT power. It was concluded that for this system with |skew×Rs| $>>1$, a DFB laser needed a margin of about 8 dB of ICXT level to have the same outage probability of a system using ECL.

2.5. Summary

In section 2.1, the growth of interconnections in data centers over the last few years and the need to increase data center rates without increasing cost are described. Section 2.2, presents the SDM technology. In subsection 2.2.3, MCFs are showed as a solution to increase the bit rate without increasing bandwidth, and to enable scalability while improving the space utilization in data centers. Section 2.3, describes the KK receiver. It shows that, although DD is used, the receiver can be linearized. It is also shown that, with the KK receiver has a low cost, as only need a single PD, without lowering the system performance. Finally, in section 2.4, the phase noise is described, and some studies, assessing the impact of the laser phase noise on MCFs and KK receivers, are shown.

Chapter 3
System description

In this chapter the architecture of the system used in this work is presented. The models used in the simulations are also presented and validated in this chapter. Finally the metrics to evaluate the system performance are described.

3.1. System architecture

Figure 4 shows the system model and how each component of the simulator was used. In this work, a 16-QAM signal with a bit rate of 240 Gbit/s is considered. After the signal generation, the 16-QAM signal is sampled and passed through a root-raised-cosine filter. After the filter, the signal is converted to the optical domain using a dual parallel Mach-Zehnder modulator (DP-MZM) without generating a carrier. After the signal is modulated it is shifted by at least B/2 to ensure that when the carrier is added it is in the leftmost of the signal. After the shift, the carrier is added to get a SSB signal that is launched into the optic fiber.

In the MCF, the linear propagation is considered and the ICXT from the interfering core is added to the interfered core. This will be discussed in detail in subsection 3.3. Finally, the signal reaches the detection phase where, using the KK receiver, the optical signal is converted to an electrical signal and the electrical noise is added to the signal. Then the chromatic dispersion is compensated and the electrical signal is passed through a RRC filter. Finally, the signal reaches the decision phase where the EVM and BER are evaluated.

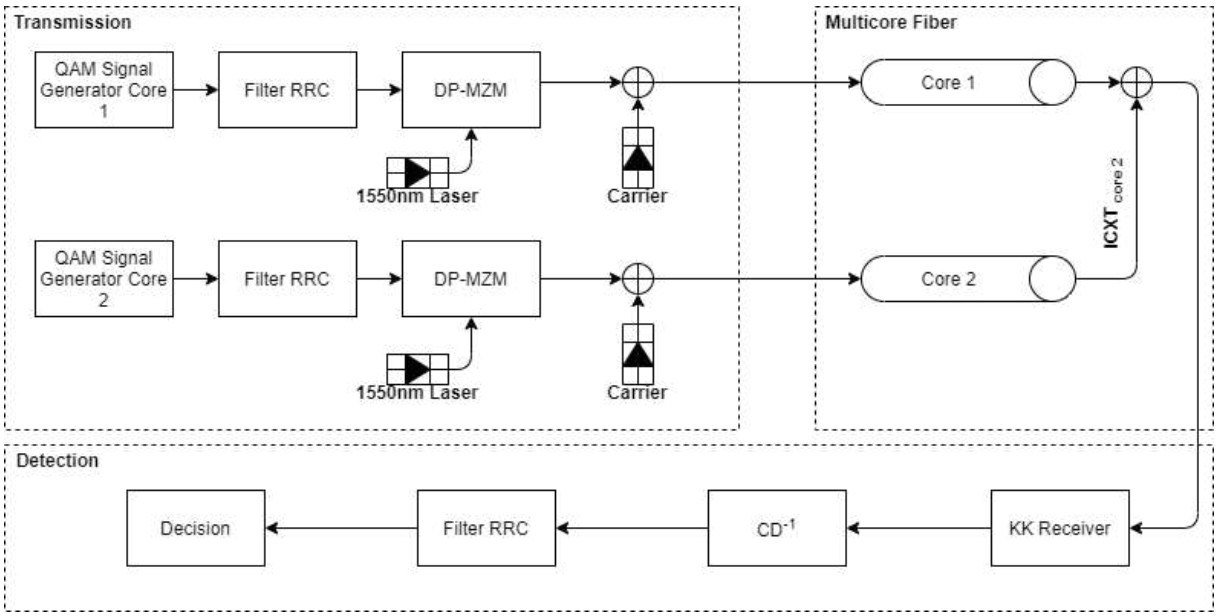

FIGURE 4. System model.

3.2. Transmission model

3.2.1. Filter model

As stated above, after generating the QAM signal, the next step is to pass it through a root-raised cosine (RRC) filter to minimize the intersymbol interference (ISI). This is done in two steps, at the transmission after the QAM signal is generated and after the chromatic dispersion compensation in the detection phase. This way the signal at the detection phase has a raised cosine shape reducing the interference caused by the ISI in the optimal sample time.

$$H_{rc}(f) = \begin{cases} 1, & |f| \leq \frac{1-\beta}{2T} \\ \frac{1}{2}\left[1 + \cos(\frac{\pi T}{\beta}\left[|f| - \frac{1-\beta}{2T}\right])\right], & \frac{1-\beta}{2T} < |f| \leq \frac{1+\beta}{2T} \\ 0, & \text{otherwise} \end{cases} \tag{3.1}$$

To obtain the transfer function of the RRC filter, first we obtain the transfer function of the raised-cosine filter using 3.1, where β is the roll-off factor of the filter and T_s is the symbol period. Afterwards, to get the transfer function of the RRC filter (H_{rrc}) we take the square root of the raised-cosine transfer function ($\sqrt{H_{rc}}$). In this work a roll-off factor of 0.01 was used for all simulations.

3.2.2. Modulator model

In this work, a DP-MZM is used. The DP-MZM is an IQ modulator that is able to convert the I and Q components of the electrical signal into the optical domain. The DP-MZM has two arms, one for the in-phase component of the QAM signal and the other for the quadrature component, employing a MZM modulator for each arm. The DP-MZM modulator is depicted in Figure 5. The DP-MZM operation is described in 3.2, 3.3 and 3.4, defining the characteristic of the modulator.

$$e_{out}(t) = \frac{E_{in}}{2}[\exp\left(j\frac{\pi}{2V_{sv}}V_{b,3}\right)\frac{e_1(t)}{E_{in,1}} + \exp\left(-j\frac{\pi}{2V_{sv}}V_{b,3}\right)\frac{e_2(t)}{E_{in,2}}] \tag{3.2}$$

$$e_{1,2}(t) = \frac{E_{in,1,2}}{2}[\exp\left(j\frac{\pi}{2V_{sv}}V_{1,2}\right) + \exp\left(-j\frac{\pi}{2V_{sv}}V_{1,2}\right)] \tag{3.3}$$

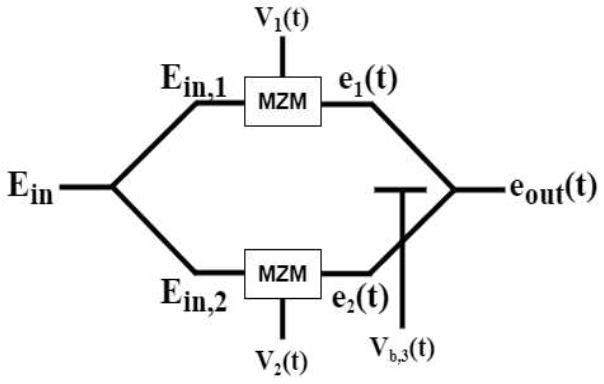

FIGURE 5. DP-MZM model.

$$V_{1,2} = V_{b(1,2)} + v_{I,Q}(t) \tag{3.4}$$

Equation 3.2 shows the field at the DP-MZM output. E_{in} is the optical field at DP-MZM input. V_{sv} is the switching voltage with a typical value of 3.5 V. $V_{b,1}$, $V_{b,2}$ and $V_{b,3}$ are the bias voltages. The fields in the upper and lower arm are given by equation 3.3. $E_{in,1,2}$ are the fraction of the signal at the DP-MZM input that are applied to the inner MZMs.
Considering that the carrier will be added later, to ensure that the signal is generated without a carrier it is necessary that both the upper and lower arms do not generate one. For this reason, the bias voltage of the inner MZMs must be at the minimum bias point. Furthermore, equation 3.3 can be simplified as equation 3.5 using the complex cosine simplification.

$$e_{1,2}(t) = \cos\left(\frac{\pi}{2V_{sv}}V_{1,2}\right)E_{in,1,2} \tag{3.5}$$

Assuming a $V_{1,2} = -V_{sv} + v_{I,Q}(t)$ (minimum bias point), we can further simplify the equation to equation 3.6:

$$e_{1,2}(t) = \cos\left(\frac{\pi}{2V_{sv}}(-V_{sv} + v_{I,Q}(t))\right)E_{in,1,2} \tag{3.6}$$

After manipulating the equation 3.6 and assuming the linerized MZM is at the minimum bias point to avoid non-linear effects, the field at the output of any given arm of the DP-MZM is given by:

$$e_{1,2}(t) = \frac{\pi}{2V_{sv}}v_{I,Q}(t) \tag{3.7}$$

For $V_{b,3}$, the outer MZM, it needs to be biased at the quadrature point. This is the only point that guarantees that the upper arm and lower arm fields are out of phase by $\frac{\pi}{2}$ radians. This will generate the in-phase and quadrature component of the signal. Using the result of 3.7 and simplifying equation 3.2, assuming the linearized MZM, no insertion loss and $E_{in,1} = E_{in,2} = \frac{E_{in}}{2}$,the DP-MZM modulator equation is given by:

$$e_{out}(t) = \frac{E_{in}}{2}e_1(t) + j\frac{E_{in}}{2}e_2(t) \tag{3.8}$$

To create the SSB signal depicted in figure 6, the carrier needs to be generated and added to the signal. To accomplish this the signal needs to be shifted by at least half of the signal band and then the generated carrier in base band is added. With this, we obtain a signal in the same form as the equation 3.9, where A is the carrier, $S(t)$ is the signal after the IQ modulator and is given by equation 3.8, $\frac{B}{2}$ is the spectral shift applied to the signal and $\phi(t)$ is the phase noise associated with the laser imperfections.

$$E(t) = [A + S(t)e^{j\pi\frac{B}{2}t}]e^{j\phi(t)} \tag{3.9}$$

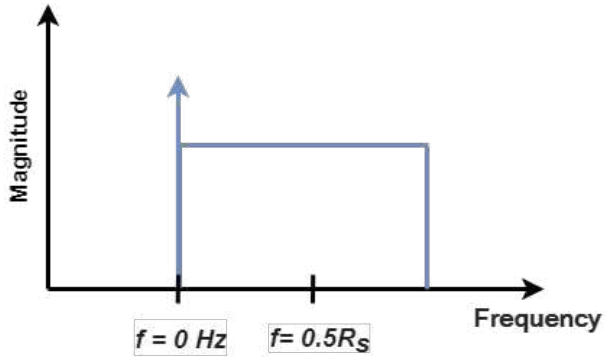

FIGURE 6. Ideal SSB signal.

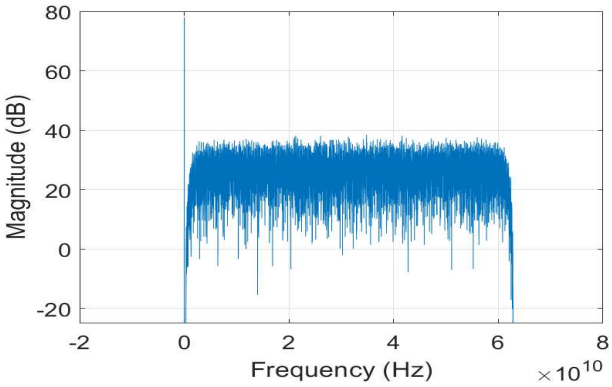

FIGURE 7. Magnitude of the spectrum of the SSB signal obtained by simulation.

Figure 7 shows the spectrum of the SSB signal in base band after inserting the carrier. These results do not consider phase noise. Without any impairments the spectrum is shown to be close to figure 6, the ideal spectrum.

3.2.3. Laser phase noise

As said in chapter 2, the phase noise is derived from the laser imprecision. Since it is impossible to emit only one frequency there is always spectral width associated with each optical emitter [**33**]. In the field of optical communications, the two most common used types of lasers are the ECL (external cavity laser) and the DFB (distributed feedback laser). The ECL have a lower spectral width, around 100 kHz, but higher cost, while the DFB have a lower cost but higher spectral width (typical value of few MHz). For this work, it is more interesting to analyze the impact that a low cost with high spectral width laser has on the system performance, as the system is designed to be as low cost as possible.

The phase noise is generally modelled by a Brownian motion, with zero mean and variance given by $2\pi\Delta\upsilon_l t$, where $\Delta\upsilon_l$ is the spectral width of the laser at -3 dB. This is a Wienner process, characterized by equation 3.10 [**36**]:

$$\phi(t) = 2\pi \int_0^t n(\tau)d\tau \tag{3.10}$$

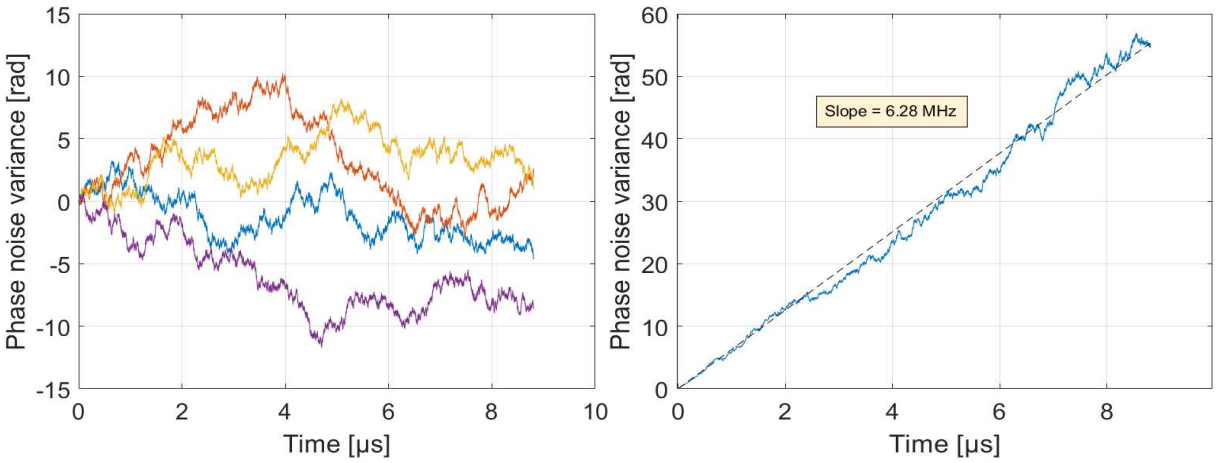

(a) Four phase noise samples. (b) Phase noise variance.

FIGURE 8. Four phase noise samples (a) and variance of 150 samples of phase noise (b) as function of time with $\Delta\upsilon_l = 1$ MHz.

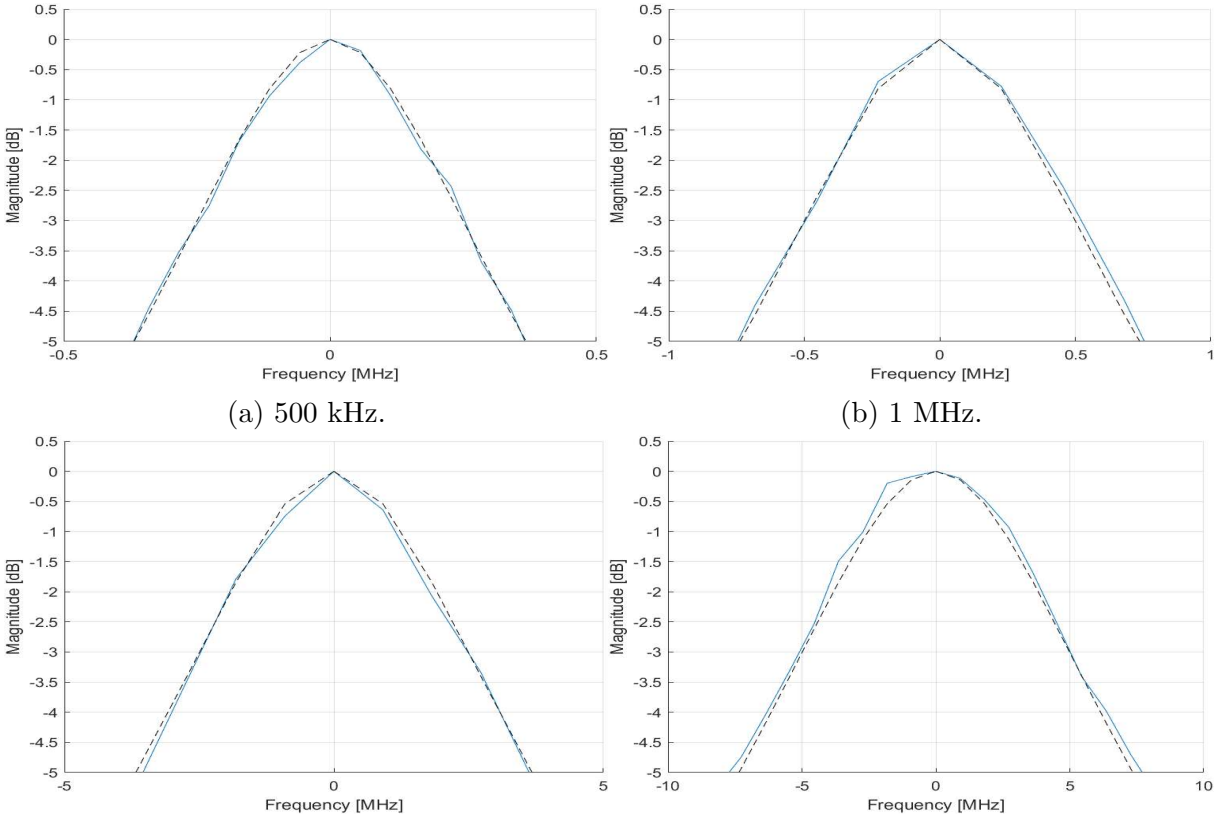

(a) 500 kHz. (b) 1 MHz.

(c) 5 MHz. (d) 10 MHz.

FIGURE 9. Spectrum of the electrical field at the laser with different linewidths: (a) 500 kHz,(b) 1 MHz,(c) 5 MHz,(d) 10 MHz.

Where $n(\tau)$ is white gaussian noise with zero mean and variance of $\Delta\upsilon_l/2\pi$.
Figure 8a shows four different samples of the phase noise process with 1 MHz of linewidth. It is shown that each phase noise sample has an independent walk from the other samples. Figure 8b shows the variance of the phase noise process for a laser with a linewidth of 1 MHz. To estimate the variance, 1000 samples of the phase noise process were generated.

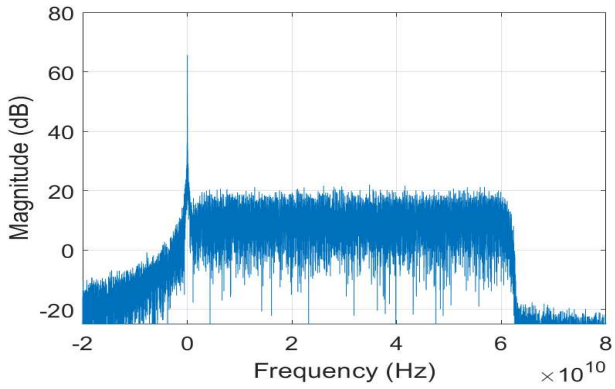

FIGURE 10. Power spectral density of the SSB 16-QAM signal at transmitter considering the laser phase noise.

The expected value of the slope (dashed line) should be equal to $2\pi\Delta v_l$. For a laser with 1 MHz this is 6.28 Mrad/s. As expected, the variance has a good approximation with the theoretical value.

Figure 9 represents several spectrum of the electrical field at the laser for different lasers with different linewidths. The linewidth for all lasers is measured at half power, i.e. -3 dB. Since the spectrums are normalized (i.e. the max value of the spectrum is at 0 dB) this means we can verify each linewidth by taking the value at -3 dB. Figure 9 shows that the laser spectrum are good approximations of the theoretical model (dashed line) [**37**].

After taking into account a laser with 1 MHz of linewidth and considering the laser phase noise, we obtained the SSB signal in the simulation shown in figure 10. Comparing with the signal without the phase noise (shown in figure 7), it is visible that the carrier is no longer a single dirac in the spectrum. It is also noted that the magnitude of the signal is more spread across the band.

3.3. MCF model

In this work we used the model expressed in [**38**]. The discrete changes model (DCM) evaluates the ICXT considering the two polarization directions of interfered core and an interfering core. This model is convenient because the DCM includes differences between the cores refractive indexes [**38**], the dual polarization [**39**] and random variations of the ICXT over time [**40**] [**41**]. For the implementation of the model first we divide the field power between the two polarizations. In this work we assume the simple case in which the x and y polarizations contain half of the total signal power. Then linear propagation is considered in the interfered core using equation 3.11.

$$H(f) = \exp\left(-j\beta_0 L - j\beta_1\omega L - j\frac{\beta_2}{2}\omega^2 L - j\frac{\beta_3}{6}\omega^3 L\right)\exp\left(-\alpha\frac{L}{2}\right) \tag{3.11}$$

Where L is the fiber length, ω is the angular frequency, β_0, β_1, β_2 and β_3 are given by equations 3.12, 3.13, 3.14, 3.15 and α is the attenuation coefficient of the fiber.

$$\beta_0 = \frac{n_{eff}2\pi}{\lambda_0} \tag{3.12}$$

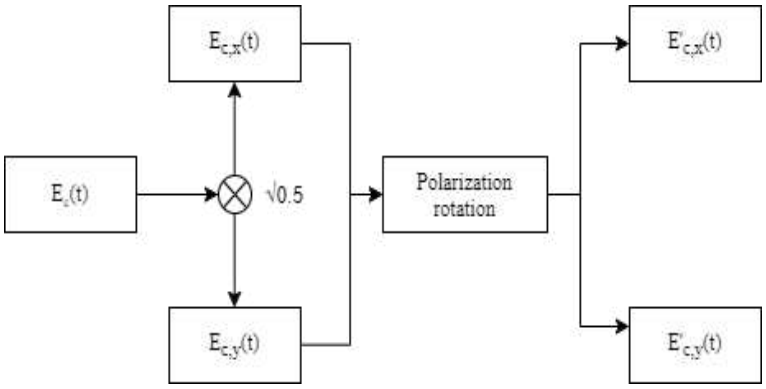

FIGURE 11. Block diagram of the rotation of the polarization.

$$\beta_1 = \frac{n_{eff}}{c} \tag{3.13}$$

$$\beta_2 = -\frac{D_{\lambda 0}\lambda_0^2}{2\pi c} \tag{3.14}$$

$$\beta_3 = S_{\lambda_0}\left(\frac{\lambda_0^2}{2\pi c}\right)^2 + \frac{D_{\lambda 0}\lambda_0^3}{2\pi^2 c^2} \tag{3.15}$$

In equations 3.12, 3.13 3.14 and 3.15, n_{eff} is the effective refractive index of the core, λ_0 is the operating wavelength, c is the speed of light, $D_{\lambda 0}$ is the dispersion parameter at the wavelength λ_0 and S_{λ_0} is the slope of the dispersion parameter at the wavelength λ_0.

Fiber transmission also includes random polarization rotation. This is modeled by 3.16 and 3.17 [**19**].

$$E'_{n,x}(t) = e^{j\theta}cos(\Gamma)E_{n,x}(t) - e^{-j\psi}sin(\Gamma)E_{n,y}(t) \tag{3.16}$$

$$E'_{n,y}(t) = e^{j\psi}sin(\Gamma)E_{n,x}(t) + e^{-j\theta}cos(\Gamma)E_{n,y}(t) \tag{3.17}$$

Where the phases ψ, Γ and θ are random processes between 0 and 2π, and $E_{n,x}$ and $E_{n,y}$ are the fields without considering rotation.

Figure 11 depicts how the rotation is performed in the system. Given the signal on a given core c ($E_c(t)$), its power is divided among the two polarizations, in this case half for each. Afterwards the polarization rotation is performed using equations 3.16 and 3.17.

After the polarization rotation the DCM model is used to calculate the ICXT field. The ICXT field of the interfered core can be written as [**39**]:

$$E_{ICXT}(t) = E_{ICXT,x}(t)\hat{x} + E_{ICXT,y}(t)\hat{y} \tag{3.18}$$

Where $E_{ICXT,x}(t)$ and $E_{ICXT,y}(t)$ are the field component given by:

$$E_{ICXT,x}(t) = \mathfrak{F}^{-1}[E_{m,x}(\omega)F_{x,x}(\omega)] + \mathfrak{F}^{-1}[E_{m,y}(\omega)F_{y,x}(\omega)] \tag{3.19}$$

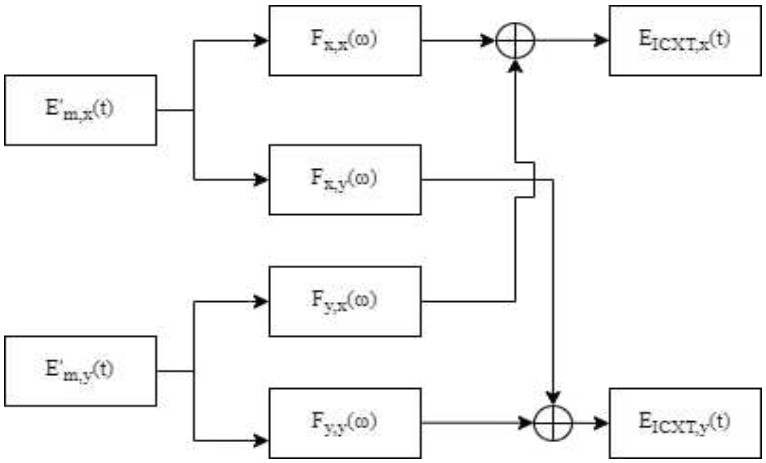

FIGURE 12. Block diagram of the generation of the ICXT fields.

$$E_{ICXT,y}(t) = \mathfrak{F}^{-1}[E_{m,x}(\omega)F_{x,y}(\omega)] + \mathfrak{F}^{-1}[E_{m,y}(\omega)F_{y,y}(\omega)] \tag{3.20}$$

Where $E_{m,x}(\omega)$ and $E_{m,y}(\omega)$ are the field components from the interfering core in the frequency domain, $\mathfrak{F}^{-1}$ is the inverse fourier transform and $F_{p,b}(\omega)$ are the functions that model the ICXT.

Figure 12 depicts how the field components are obtained using this model. To generate each field polarization of the ICXT four independent $F_{p,b}(\omega)$ functions are generated using equation 3.21, each one referring to a different field component. After generating the $F_{p,b}(\omega)$, the equations 3.19 and 3.20 are used to obtain the IXCT field, which will be added to the interfered signal field to obtain the final signal with the ICXT. The functions $F_{x,x}(\omega)$ and $F_{x,y}(\omega)$ describe the impact that the interfering core has on the x-polarization of the interfered core and the functions $F_{y,x}(\omega)$ and $F_{y,y}(\omega)$ refer to the impact of each polarization of the interfering core on the y-polarization of the interfered core.

$$F_{p,b}(\omega) = -j\frac{\overline{K}_{nm}}{\sqrt{2}}H_n(f)\sum_{k=1}^{N} e^{(-j\Delta\overline{\beta}_{mn}(\omega)z_k)}e^{(-j\phi_{p,b}^{(k)})} \tag{3.21}$$

The $\overline{K}_{nm}$ is the coupling coefficient, it can be obtained assuming a ICXT level (X_c) and using equation 3.22 to evaluate it.

$$X_c = N|\overline{K}_{nm}|^2\frac{P_m}{P_n} \tag{3.22}$$

Where P_m and P_n are the power in the interfering and interfered cores respectively and N is the number of phase-matching points (PMPs). PMPs are the number of points along the MCF where the difference between effective refractive indexes of the interfering and interfered cores is zero [**40**]. The z_k is a random variable uniformly distributed between $\frac{(k-1)L}{N}$ and $\frac{kL}{N}$ where N is the number of PMPs. $\phi_{p,b}^{(k)}$ are random phase shifts (RPS) that model physical conditions of the MCF. RPS are random variables uniformly distributed between 0 and 2π and are what gives a random fluctuation for each PMP. The $\Delta\overline{\beta}_{mn}(\omega)$

is the difference between the averages of the propagation constants, and is obtained with equation 3.23.

$$\Delta\overline{\beta}_{mn}(\omega) = \Delta\overline{\beta}_{0,mn} + d_{mn}\omega - \Delta D_{mn}\frac{\lambda^2\omega^2}{4\pi c} \tag{3.23}$$

Where $\Delta\overline{\beta}_{0,mn}$ is the difference between the averages of the propagation constants at $\omega = 0$, d_{mn} is the average walkoff parameter between both cores, ΔD_{mn} is the difference between the dispersion parameter for both cores, λ is the carrier wavelength, ω is the angular frequency given by $\omega = 2\pi f$ and c is the speed of light.

To evaluate the stochastic proprieties of each time fraction the short-time average crosstalk (STAXT) is evaluated. The STAXT is the average value of the ICXT for a short period of time that usually is much smaller than the decorrelation time of the MCF (on the order of a few minutes) [**41**]. In this work, that short period of time is designated by time fraction. Each time fraction has a value between 200 ns and 1000 ns depending on the number of bits sent. Since it is far less than the decorrelation time of the MCF, we can assume that throughout its duration the value of the ICXT is constant, and the polarization rotation phases (ψ, Γ and θ) have a constant value [**19**]. To calculate the STAXT equation 3.24 is used.

$$STAXT_n(t) = \frac{1}{T}\int_{t-T}^{t} |E_{ICXT}(t)|^2 dt \tag{3.24}$$

Where T is the duration of the time fraction and $E_{ICXT}(t)$ is the ICXT field.

In this work the instantaneous ICXT power $p_{icxt}(t)$ is also evaluated. The instantaneous ICXT power gives the information about how the ICXT power behaves in the duration of a time fraction. The instantaneous ICXT power is given by equation 3.25.

$$p_{icxt}(t) = |E_{ICXT,x}(t)|^2 + |E_{ICXT,y}(t)|^2 \tag{3.25}$$

Where $E_{ICXT,x}(t)$ and $E_{ICXT,y}(t)$ are the ICXT field at their respective polarizations directions.

3.3.1. ICXT model validation

To validate the ICXT model implemented in the simulator, the probability density functions of the four ICXT field components were obtained by simulation and compared with the theoretical Gaussian PDFs presented in [**39**]. Figure 13 depicts the probability density function of the ICXT field for all components. It is concluded that all components have similar forms as expected and shown in [**39**]. The theoretical Gaussian PDF is also presented for comparison. The mean of the theoretical PDF is obtained using the relation between the amplitude of the I and Q components and their respective variances, $\langle XT_x\rangle = \sigma^2_{x,I} + \sigma^2_{x,Q}$ and $\langle XT_y\rangle = \sigma^2_{y,I} + \sigma^2_{y,Q}$. Thus, to get the mean of the ICXT we use: $\langle XT\rangle = \sigma^2_{x,I} + \sigma^2_{x,Q} + \sigma^2_{y,I} + \sigma^2_{y,Q}$

In order to verify that the ICXT power is well calculated it is also possible to get the value with: $\langle XT\rangle = N|\overline{K}_{nm}|^2 P_m$ as shown in [**39**]. Figure 14 depicts the average of the

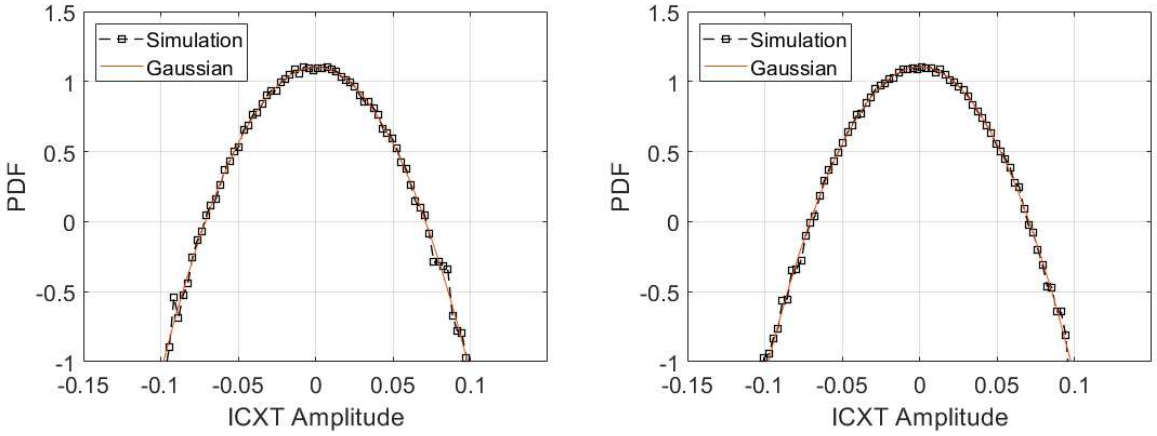

(a) In-phase component of $ICXT_x$.

(b) Quadrature component of $ICXT_x$.

(c) In-phase component of $ICXT_y$.

(d) Quadrature component of $ICXT_y$.

FIGURE 13. PDF of the ICXT field components: a) I component of the x direction, b) Q component of the x direction, c) I component of the y direction, d) Q component of the y direction

STAXT power for a number of time fractions, when the number of time fractions is 1, only 1 time fraction is used to get the average of the STAXT value. When the number of time fractions is 500, 500 time fractions were used to calculate the average STAXT value. After 500 time fractions with an ICXT level of -15 dB and a P_m equal to -9 dBm we can confirm that this value has been reached, as seen in figure 14.

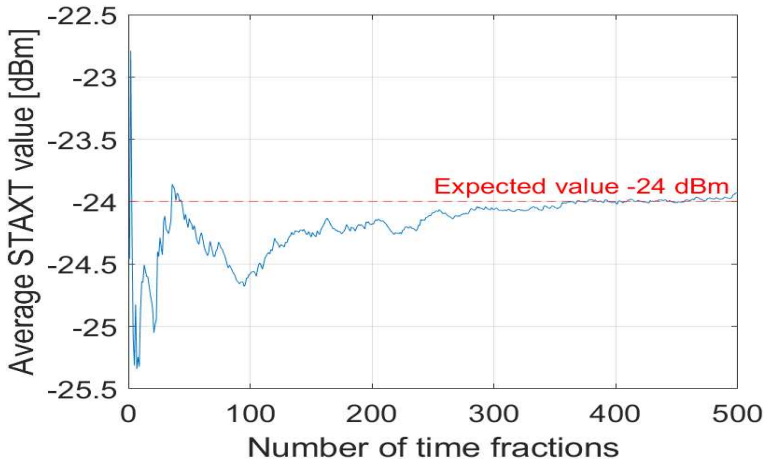

FIGURE 14. Average STAXT per time fraction used.

3.4. Receiver model

In this section the optical receiver model used in this work is described and validated.

3.4.1. Optical receiver

As mentioned in chapter 2, this system employs direct detection to have a cost-effective solution. This implies the use of a single PD to detect the signal intensity. The following equation expresses the detected SSB signal assuming no transmission impairments.

$$i(t) = R_\lambda |e(t)|^2 = R_\lambda (|A|^2 + A^* \cdot S(t) e^{j\pi Bt} + A \cdot S^*(t) e^{-j\pi Bt} + |S(t)|^2) \tag{3.26}$$

Where $i(t)$ is the electric current after photodetection, R_λ is the responsivity of the PIN, $e(t)$ is the optical field after the MCF output, A is the optical carrier, B is the spectral shift and $S(t)$ is the information signal. In equation 3.26, the part containing the information ($A^* \cdot S(t) e^{j\pi Bt}$) and the SSBI ($|S(t)|^2$) are in band interfering with each other. If the SSBI is removed then the information signal can be retrieved using a single PD. As explained in section 2, the technique used in this work for the signal detection was the KK field reconstruction which only requires that the SSB signal satisfies the minimum phase condition. If so, the information signal phase can be extracted from the signal amplitude using the KK relation expressed in 3.27:

$$\varphi(t) = 0.5 \cdot \boldsymbol{H}(\ln(|i(t)|^2)) \tag{3.27}$$

Where $\boldsymbol{H}$ is the Hilbert transform. In this work this was implemented in the frequency domain as shown in [**42**]. By using the phase of the signal it is possible to recover the full information signal [**2**] from:

$$S(t) = (\sqrt{i(t)} e^{j\varphi(t)} - A) e^{-j\pi Bt} \tag{3.28}$$

Equation 3.4.1 shows that after the KK relation and the removal of the carrier A, as long we know initial frequency shift B we can recover the original signal.

After the KK receiver and the removal of the carrier, the chromatic dispersion compensation is performed. In this work, the CD is perfectly compensated using the inverse of the optic fiber model, $\frac{1}{H(f)}$. Afterwards, the signal passes through the matching RRC filter and the final symbol decision can be performed.

3.4.2. Receiver model validation

Parameter	**Symbol**	**Valeu**
Bit rate	R_b	240 Gbit/s
Modulation	M	16-QAM
Signal power at the KK input	P_{in}	0 dBm
CSPR	$CSPR$	13 dB
PAPR	$PAPR$	6.38 dB

TABLE 2. KK receiver validation parameters.

Table 2 shows the important values used for this validation. The R_b is the bit rate used, M is the modulation order of the QAM signal used, the P_{in} is the signal power at the input of the KK receiver. The $CSPR$ is the carrier-to-signal power ratio, given by:

$$CSPR = \frac{|A|^2}{|S(t)|^2} \tag{3.29}$$

Where A is the carrier and $S(t)$ is the information signal.
The $PAPR$ is the peak-to-average power ratio and is given by:

$$PAPR = \frac{\max(|S(t)|^2)}{|S(t)|^2} \tag{3.30}$$

To validate the KK model, we need to verify the minimum phase condition. To guarantee the condition it is necessary that the $CSPR$ is larger than the $PAPR$ [**24**]. This can be understood as when this relation is met, the time trajectory of SSB signal does not include the origin [**8**].

Figures 15, 16 and 17 show the time trajectory of the SSB signal and its respective constellation after the detection through the KK algorithm. All results were done assuming a B2B case without electrical noise, ICXT or laser phase noise. Figure 15a shows that for this case the minimum phase condition is met, as the time trajectory does not include the origin. This is to be expected since the CSPR is greater than the PAPR. Figure 15b shows the constellation of the SSB signal after the KK algorithm (blue dot) and the ideal constellation (red cross). When the minimum phase condition is met the constellation shows that the simulation and the ideal case are exactly the same. Figure 16a depicts the time trajectory of the signal when the CSPR is equal to the PAPR. As

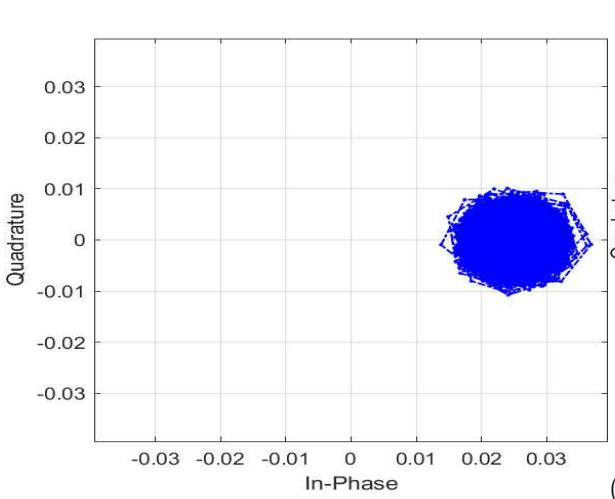

(a) Time trajectory of SSB signal.

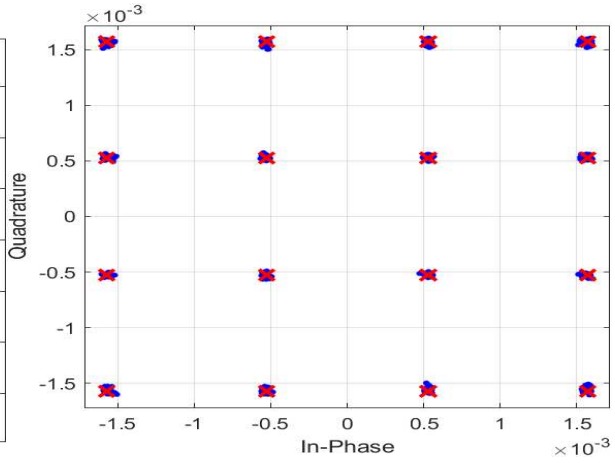

(b) Constellation detected after the KK algorithm.

FIGURE 15. SSB signal time trajectory and constellation for CSPR = 13 dB and PARP = 6.38 dB.

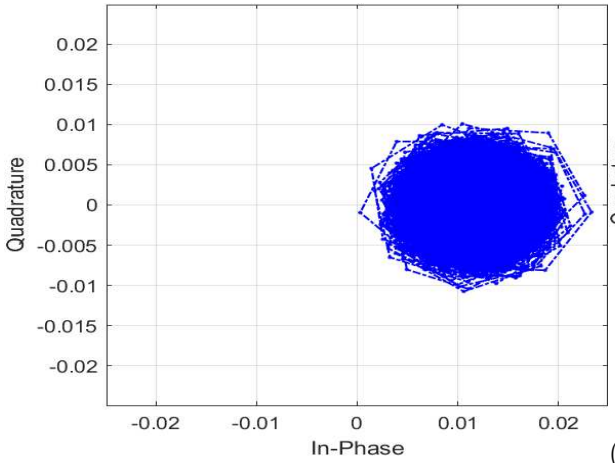

(a) Time trajectory of SSB signal.

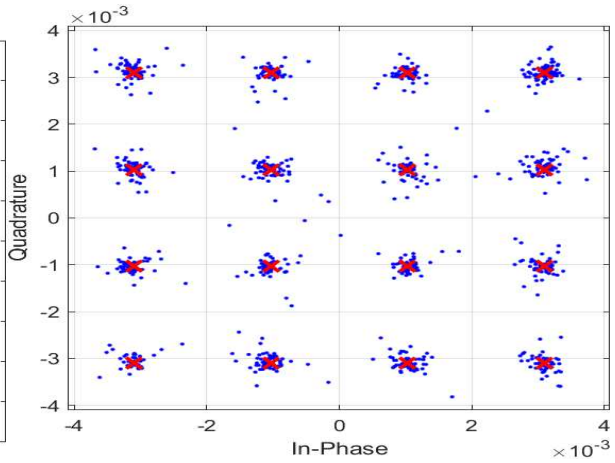

(b) Constellation detected after the KK algorithm.

FIGURE 16. SSB signal time trajectory and constellation for CSPR = 6.38 dB and PARP = 6.38 dB.

shown in this case the origin is almost inside the time trajectory of the signal. This is expected as this is the value of CSPR that begins to meet the minimum phase condition. Figure 16b depicts the constellation of the SSB signal after the KK algorithm (blue dot) and the ideal constellation (red cross). It is concluded that with this CSPR it is possible to retrieve the final constellation, although the result will be degraded. Figure 17a shows the time trajectory of the SSB signal when the minimum phase condition is not met, i.e. the PAPR is greater than the CSPR. In this case multiple time trajectories will encircle the origin and therefore the minimum phase condition will not be met. Figure 17b shows the constellation of the SSB signal after the KK algorithm (blue dot) and the ideal constellation (red cross). It is shown that when the minimum phase condition is not met the SSB signal constellation will be degraded to the point that the signal is not retrievable.

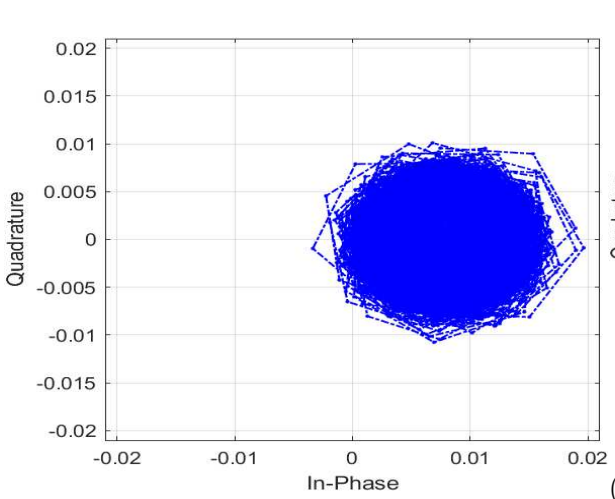

(a) Time trajectory of SSB signal.

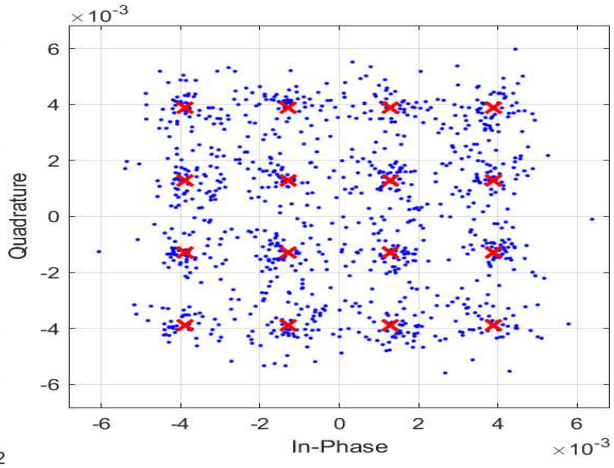

(b) Constellation detected after the KK algorithm.

FIGURE 17. SSB signal time trajectory and constellation for CSPR = 3 dB and PARP = 6.38 dB.

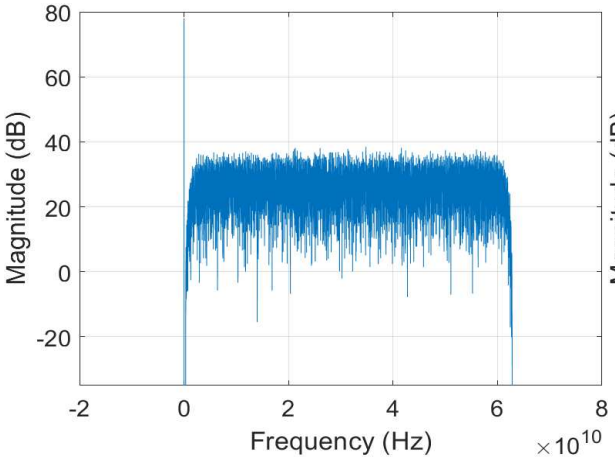

(a) SSB QAM signal at the MCF output.

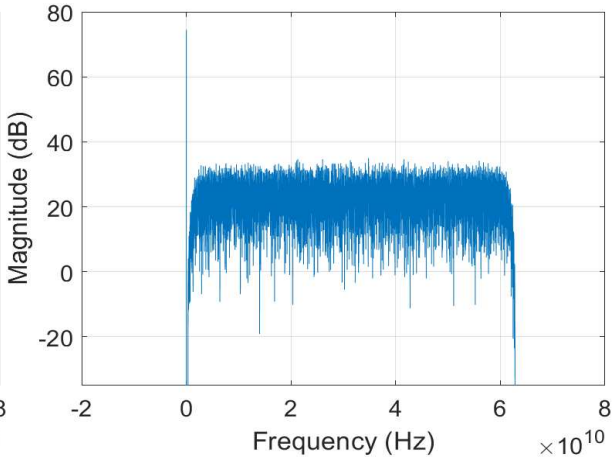

(b) SSB QAM signal after the KK receiver.

FIGURE 18. Comparison between the original and the recovered signal.

Figure 18a and 18b show the spectrum of the signal before detection (18a) and after detection and the KK algorithm 18b. To obtain these figures a B2B case is assumed without any impairments such as ICXT, laser phase noise and electric noise. These figures are similar, since there is no impairment preventing the recovery of the signal with the KK algorithm and the minimum phase condition is satisfied.

3.5. Performance evaluation

To access the system performance in this work three different metrics were used, the EVM, BER and outage probability. In this section those metrics are described.

3.5.1. Error vector magnitude

Assuming an ideal case, when a transmitter sends a symbol it is expected that its value is the same at the detection. But in practice there are always imperfections, for

example ICXT added to the signal. When considering these limitations in the system, the symbol will most likely be deviated from its expected location in the constellation. The average of these deviations for all symbols in the constellation is called the EVM (error vector magnitude). To evaluate the EVM of a constellation equation 3.31 is used.

$$\mathrm{EVM} = 10\log_{10}\left(\frac{\sum_{k=1}^{N_{sim}}|S_o(k)-S_i(k)|^2}{\sum_{k=1}^{N_{sim}}|S_i(k)|^2}\right) \tag{3.31}$$

Where N_{sim} is the total k-th number of symbols in the constellation, $S_o(k)$ is the k-th received symbol and $S_i(k)$ is the transmitted symbol.

3.5.2. Bit error rate

The bit error rate is an useful metric used to access how the system will perform. However, to obtain the system's BER a Monte Carlo simulation is often used. This is a direct count of the error by comparing the bit sent with the bit received. These simulations require not only some computing power but also a lot of time to access.

Using the EVM, a far less computing intensive and time consuming calculation, it is possible to get a theoretical value of the system's BER [**43**]. To get this theoretical value equation 3.32 [**43**] is used.

$$\mathrm{BER} = 2\frac{1-\frac{1}{\sqrt{M}}}{\log_2 M}\mathrm{erfc}\left(\sqrt{\frac{3\log_2\sqrt{M}}{M-1}\frac{1}{\mathrm{EVM}^2\log_2 M}}\right) \tag{3.32}$$

Where M is the modulation number and erfc is the complementary error function. Equation 3.32 assumes a system impaired mostly by white Gaussian noise and without any intersymbolic interference.

3.5.3. Outage probability

When the BER is higher than the FEC threshold the system is not able to correct the error and therefore the system has an outage. The outage probability (OP) is the probability that, for any given time, the variations in the impairments of the system such, as the ICXT, will have a greater impact on the BER to the point that the BER is higher than the FEC threshold. In this work a SD-FEC of 20% with a threshold of $10^{-1.8}$ was considered. To get a simulation value for the outage probability of the system for any given ICXT level value, everytime the system BER was assessed it would be compared to the FEC threshold. If the BER was higher than the FEC threshold the outage counter would increase. After the 100th outage occurrence the outage probability was calculated using equation 3.33:

$$OP = \frac{\#TF_{outage}}{\#TF_{tested}} \tag{3.33}$$

Where $\#TF_{outage}$ is the number of time fractions where the system BER was above the FEC threshold and $\#TF_{tested}$ is the total number of time fractions tested.

Chapter 4
Impact of the combined effect of ICXT and phase noise on the system performance

In this chapter, the system proposed in chapter 3 is implemented using numerical simulation. In section 4.1, the simulation parameters are stated and justified. In section 4.2, the impact of the laser phase noise on the KK receiver is studied for different scenarios. In section 4.3 the outage probability of the short-reach MCF-based system is evaluated.

4.1. System parameters

In this section the system parameters used in the simulations of this chapter are shown and justified. All simulations were done taking into account chromatic dispersion and electric noise induced by the receiver.

Parameter	**Symbol**	**Valeu**
Symbol Rate	R_s	60 Gbaud/s
Modulation	M	16-QAM
Symbols sent per time fraction	$N_{symbols}$	Variable
Samples per symbols	N_{ss}	Variable
Signal power at the MCF input	P_{in}	0 dBm
CSPR	$CSPR$	13 dB
MCF length	L	45 km
Chromatic dispersion parameter of core n	$D_{\lambda,n}$	18 ps/[nm.km]
Intrinsic effective refractive index of core n	$n_{eff,n}$	1.4453
Attenuation coefficient of core n	α_n	0.2 dB/km
Chromatic dispersion parameter of core m	$D_{\lambda,m}$	18 ps/[nm.km]
Intrinsic effective refractive index of core m	$n_{eff,m}$	1.4455
Attenuation coefficient of core m	α_m	0.2 dB/km

TABLE 3. Simulation parameters.

The bit rate, R_b, was chosen to get an exact 200 Gb/s when a soft decision forward error correction (SD-FEC) with an overhead of 20% is used. The number of symbols sent per time fraction depends on the laser linewidth used. To simulate the linewidth of the laser, a good frequency resolution is needed. So if the laser is characterized by a narrow linewidth, a greater number of symbols had to be sent per time fraction. For instance if a laser with 1 MHz was used, at least 250kHz of frequency resolution is needed. For this, we have to use at least 2^{18} symbols which leads to a frequency resolution of $\Delta f = 227$

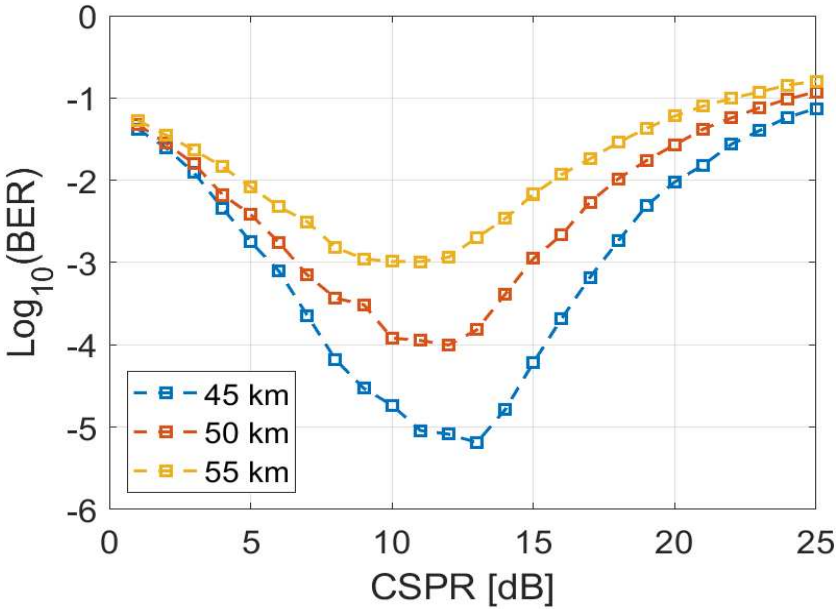

FIGURE 19. BER as a function of the CSPR for different optical fiber lengths.

kHz. Finally, the skew between cores his variable, for systems with |skew×Rs| <<1, the skew is $\frac{0.01}{R_s}$ (0.168 ps), for system with |skew×Rs| >>1, the skew is $\frac{100}{R_s}$ (1.68 ns).

Figure 19 shows the BER as a function of the CSPR for different fiber lengths. To get a high confidence for the BER result, 100 errors have been counted for each CSPR and for each fiber length. These results include the ICXT, chromatic dispersion and electrical noise effects. The simulation of the electrical noise was done as shown in appendix A. Considering a NEP (noise equivalent power) of 10 pW/Hz$^{1/2}$ and a PIN responsivity ,R_λ, of 0.8 A/W. The CSPR of 13 dB and the MCF lenght of 45 km were chosen to have an estimated BER without ICXT of 10^{-5}, as shown in figure 19.

4.2. Impact of the |skew×Rs| on the system performance without phase noise

The following studies have been performed for |skew×Rs| = 0.01 and |skew×Rs| = 100, exemplifying what happens when |skew×Rs| <<1 and |skew×Rs| >>1 respectively. In this section the impact of the |skew×Rs| on the system is assessed on the STAXT power and the instantaneous ICXT.

Figure 20 represents the STAXT for each one of the 400 time fractions tested for the case where |skew×Rs| = 0.01 and |skew×Rs| = 100. For each time fraction, the same RPS were used when simulating the two cases. With this we guarantee a fair comparison as the random ICXT is the same for |skew×Rs| = 0.01 and |skew×Rs| = 100. We can see that, in general, the value of STAXT is the same for the two cases along the 400 time fractions. The only points where there is a difference is when the value of STAXT is lower (i.e. time fraction number 96). For these time fractions the value of STAXT is lower for the case |skew×Rs| <<1 and higher for the case |skew×Rs| >>1.

Figure 21 shows the instantaneous ICXT power as a function of given time for a time fraction, considering the case where |skew×Rs| <<1 and |skew×Rs| << 1 and a CSPR

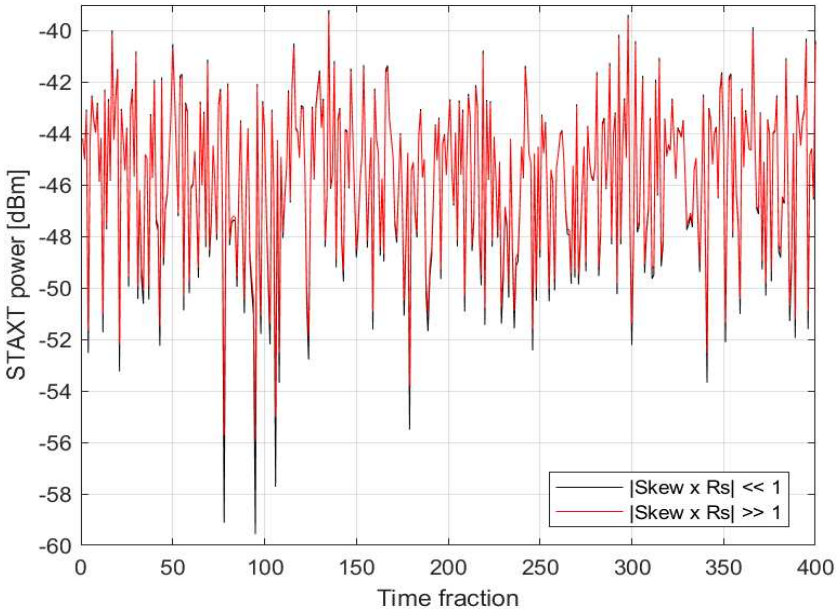

FIGURE 20. STAXT power for each time fraction when |skew×Rs| >>1 and |skew×Rs| <<1.

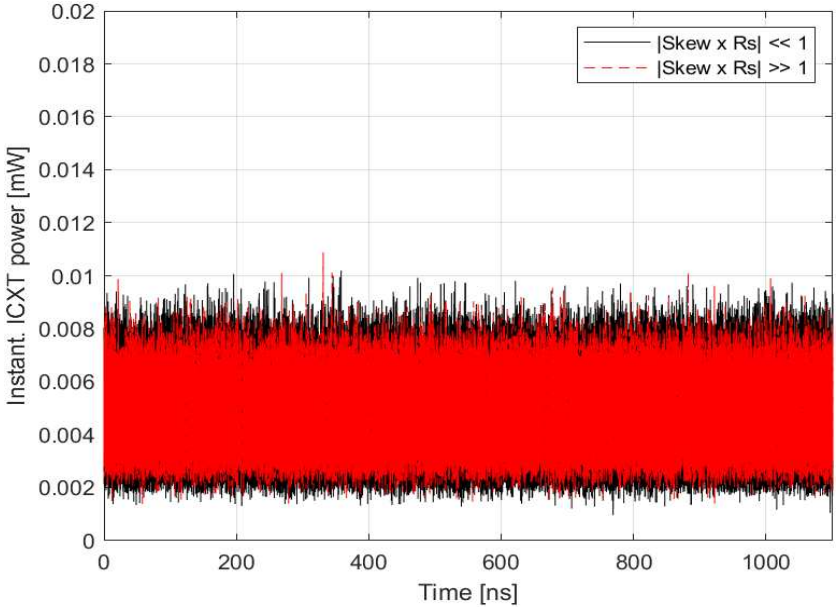

FIGURE 21. Instantaneous ICXT as a function of time when |skew×Rs| >>1 and |skew×Rs| <<1 with CSPR = 13 dB.

= 13 dB. We can observe that, in the case where |skew×Rs| >>1, the variation of the instantaneous ICXT over time is smaller compared to the case |skew×Rs| <<1. However the average of the instantaneous ICXT power tends to stay equal in both cases. These results were expected as shown in [**19**]

Figure 22 shows the instantaneous ICXT power as a function of given time for a time fraction, considering the case where |skew×Rs| <<1 and |skew×Rs| << 1 and a CSPR = 8 dB. Comparing the results with figure **??** the values of the instantaneous ICXT power have larger fluctuations. As the signal power is equal in both cases and the carrier has

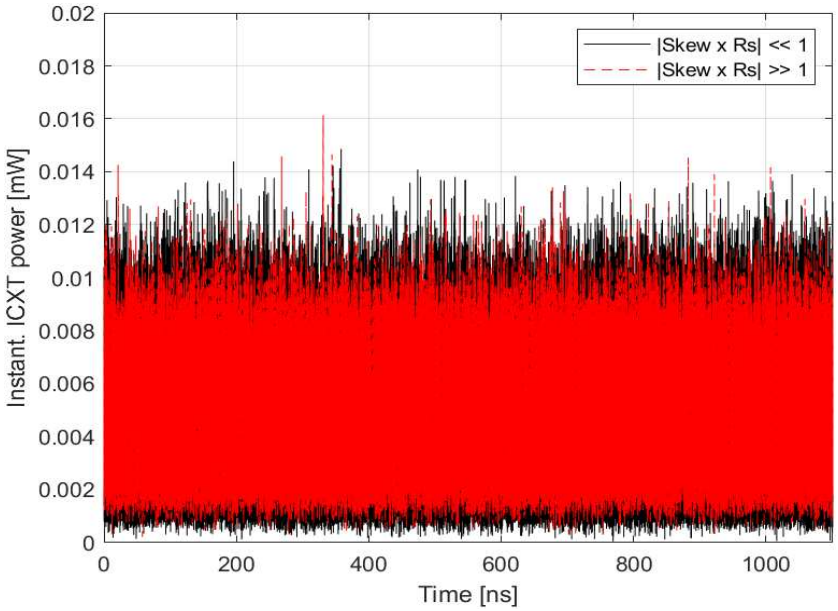

FIGURE 22. Instantaneous ICXT as a function of time when |skew×Rs| >>1 and |skew×Rs| <<1 with CSPR = 8 dB.

an lower power in comparison with the system with CSPR = 13 dB, this means the information part of the signal have an higher contribution for the ICXT power making higher fluctuations in the case with CSPR = 8 dB.

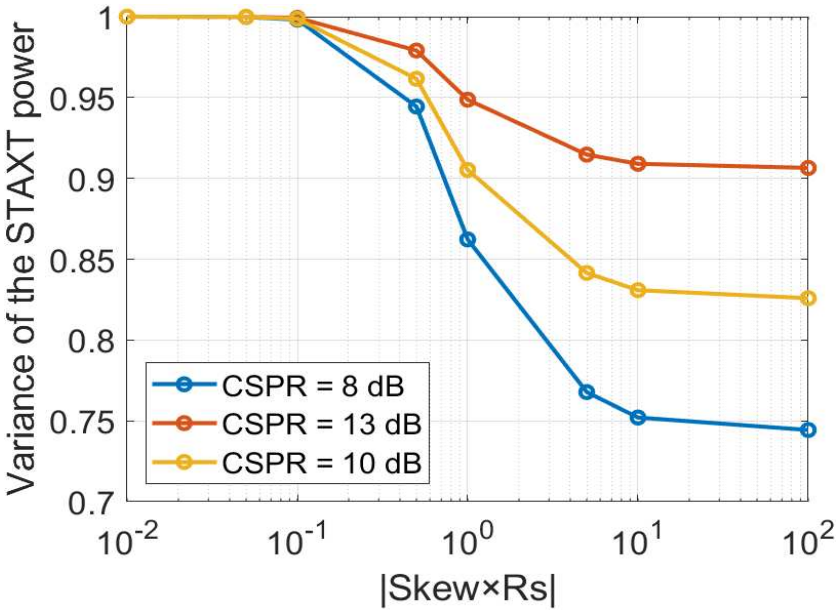

FIGURE 23. Normalized variance of STAXT as a function of the |skew×Rs| for 16-QAM modulation with different values of CSPR.

Figure 23 shows the evolution of the normalized variance of STAXT as a function of the value of the |skew×Rs| for different values of CSPR. This figure was obtained with 1000 time fractions for each value of |skew×Rs| using 16-QAM modulation. We can observe that, despite using a 16-QAM modulation, we obtained results similar to Figure 4 of [**44**]. Furthermore it is shown that for higher values of CSPR the value of the

normalized variance has a smaller discrepancy between high and low |skew×Rs|. For a CSPR of 8 dB, a reduction of 25% in normalized STAXT variance is shown, for a CSPR of 10 dB a reduction of 17% in STAXT variance is depicted and for a CSPR of 13 dB a smaller reduction of only 10% in STAXT variance is shown. As stated in [**44**], this is due to the fact that the carrier has a much stronger impact on the STAXT variance compared to all the other spectral components of the signal. This in practice means two effects are expected. (i) For low |skew×Rs| the impact of the CSPR on the STAXT variance is minimal. (ii) For higher values of |skew×Rs| the STAXT variance should be higher for signals with higher CSPR. The results shown in 21 are also confirmed, for low values of |skew×Rs| the value of the variance is greater. This would be expected since for low |skew×Rs| there are bigger fluctuations over time as shown in figure 21. In the case of |skew×Rs| <<1, the opposite happens, showing that there is a lower variation [**19**].

The result presented in figure 23 can be explained because when |skew×Rs| <<1 only one symbol will interfere in the ICXT causing constructive interactions between the different PMPs. In the case of |skew×Rs| >>1, several symbols will contribute to the ICXT, leading to a non-constructive interference between the different PMPs contributions.

4.3. Impact of the laser phase noise on the system performance

In this section the impact of the laser phase noise for the system performance is assessed. To accomplish this the STAXT for a number of time fractions and the instantaneous ICXT power as a function of time are analysed for the cases where |skew×Rs| >>1 and |skew×Rs| <<1. In the case where |skew×Rs| >>1 the cases where |linewidth×skew| <<1 and |linewidth×skew| >>1 are also studied.

4.3.1. STAXT and instantaneous ICXT power for systems with |skew×Rs| >>1

Figure 24 shows the STAXT power for 400 time fractions for the case |skew×Rs| >>1 and |linewidth×skew| <<1 for 0 MHz and 10 MHz. This result suggests that for the case where |skew×Rs| >>1 and |linewidth×skew| <<1 the laser phase noise has no impact on the STAXT power value.

Figure 25 shows the instantaneous ICXT power for time fraction 1 as a function of the time shown in figure 24. It is shown that there are no large differences between the 0 Hz laser and the 10 MHz laser, justifying why there is also no difference in the value of the STAXT in figure 24. As stated in chapter 2, this result is expected. For a case with low |linewidth×skew| it is expected that the linewidth of the laser has a small impact on the instantaneous ICXT and subsequently on the STAXT power as well. This can be justified because in the case with |linewidth×skew| <<1 the ICXT originated along the MCF will not be decorrelated by the laser phase noise, as the skew is shorter than the time interval the laser field is correlated [**35**].

Figure 26 shows the STAXT power for 400 time fractions for the case |skew×Rs| >>1 and |linewidth×skew| >> 1 when the linewidth has 10 MHz. In the reference case with

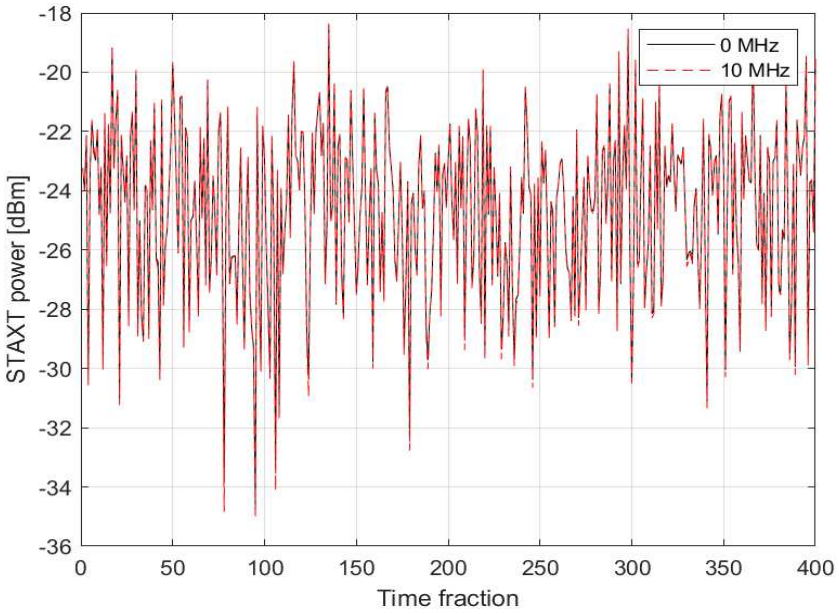

FIGURE 24. STAXT power for each time fraction when |skew×Rs| >>1 and |linewidth×skew| <<1 for an ideal laser and for a laser with linewidth of 10 MHz, assuming a skew = 1.68 ns.

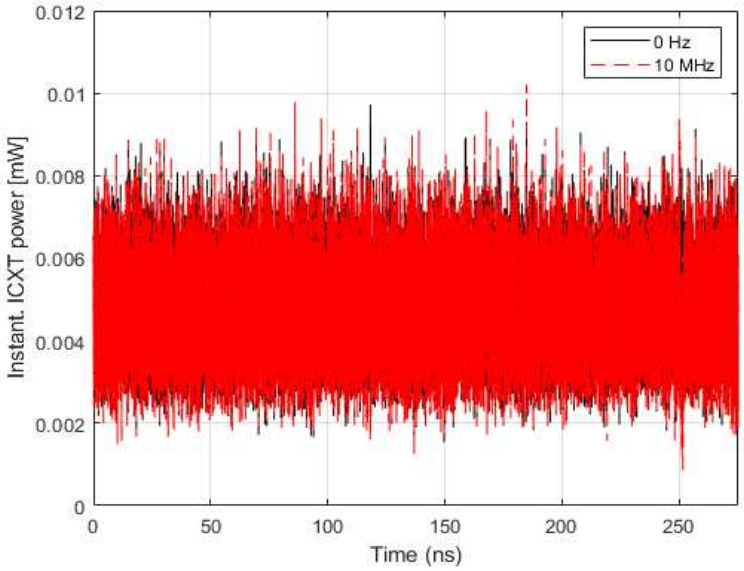

FIGURE 25. Instantaneous ICXT power as a function of time when |skew×Rs| >>1 and |linewidth×skew| <<1 for laser with 0 Hz and 10 MHz of linewidth.

0 Hz of linewidth, the system is impaired only by the ICXT and the thermal noise. In each time fraction, the same RPS were used for both linewidths to ensure that the induced ICXT is the same in the two cases. This result suggests that systems with |linewidth×skew| >> 1 (i.e. laser with 10 MHz) can significantly reduce STAXT power fluctuation. To understand this effect, let us examine what happens with the instantaneous ICXT power.

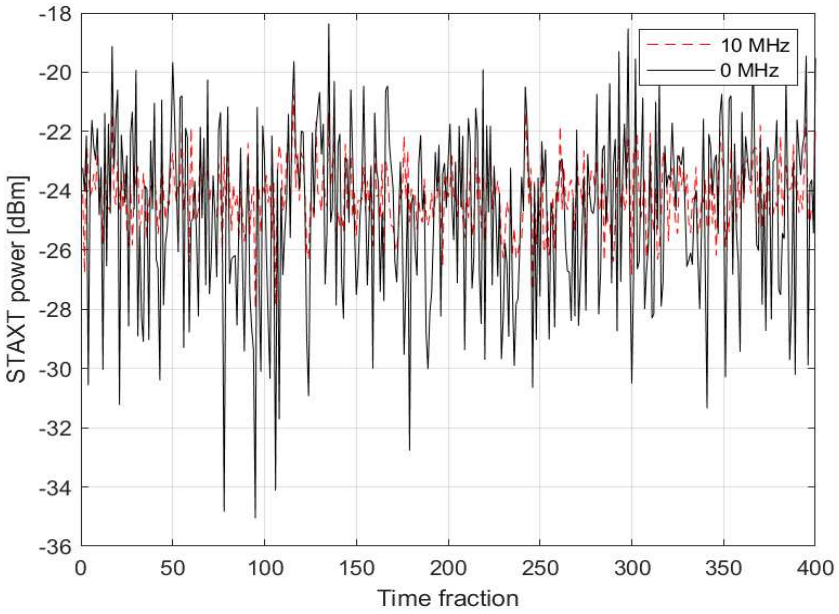

FIGURE 26. STAXT power for each time fraction when |skew×Rs| >>1 and |linewidth×skew| >>1 for a laser with linewidth of 10 MHz and an ideal laser with |skew×Rs| >>1, assuming a skew = 1.68 µs.

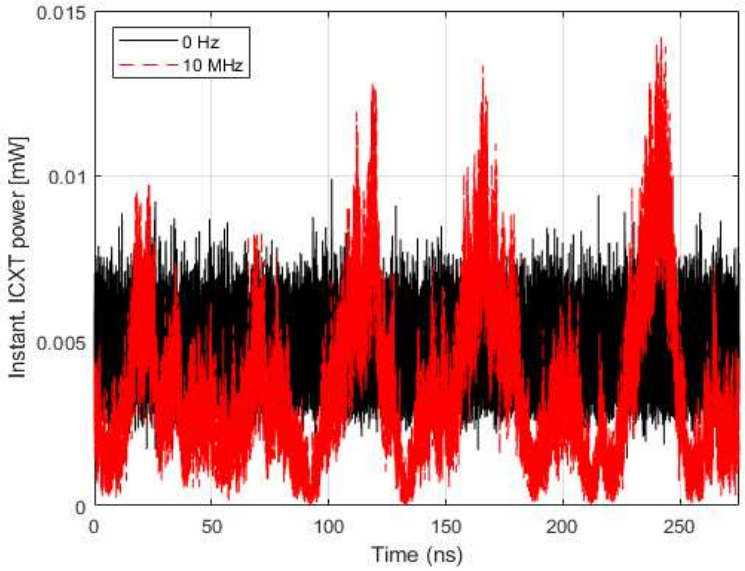

FIGURE 27. Instantaneous ICXT power as a function of time when |skew×Rs| >>1 and |linewidth×skew| >>1 for laser with 0 Hz and 10 MHz of linewidth.

Figure 27 depicts the instantaneous ICXT power as a function of time, for a given time fraction. Results for the ideal case and with a 10 MHz linewidth laser with a |linewidth×skew| >>1 are shown. We can observe that for the ideal case the value of instantaneous ICXT remains practically contained between 0.007 mW and 0.0025 mW. For a linewidth of 10 MHz there are much larger instantaneous ICXT power fluctuations which are caused by the uncorrelation induced by the phase noise on the contributions of

the ICXT originated along the MCF [**35**]. This shows that with |linewidth×skew| >>1, (i.e. the skew is longer than the time interval over which the laser field is correlated) the instantaneous ICXT variance substantially increases. Although the instantaneous ICXT power fluctuations are higher for the case where the linewidth of the laser is 10 MHz, it is more likely that the average of the instantaneous ICXT power presents small fluctuations between time fractions due to the averaging effect [**35**]. For this reason the STAXT has a smaller fluctuation for cases with higher linewidth.

4.3.2. STAXT and instantaneous ICXT power for systems with |skew×Rs| <<1

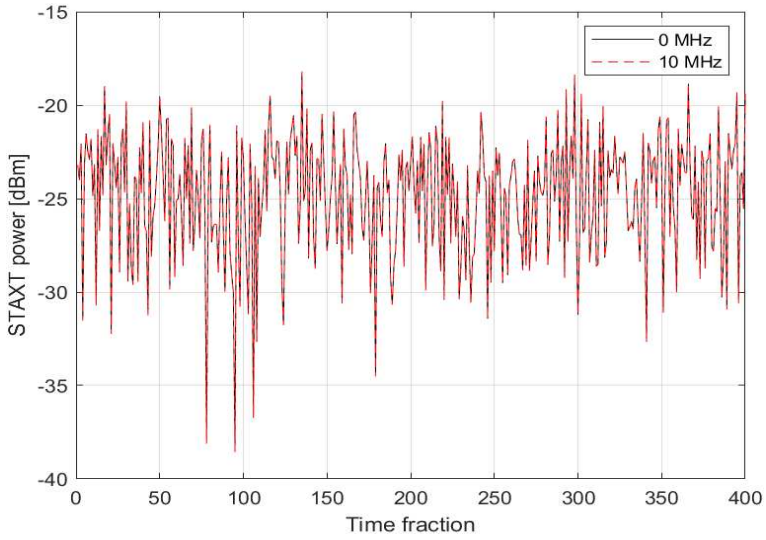

FIGURE 28. STAXT power for each time fraction when |skew×Rs| <<1 for an ideal laser and for a laser with linewidth of 10 MHz.

Figure 28 shows the STAXT power for different time fractions, for the case of 0 Hz as well as 10 MHz of linewidth. As expected from the analysis of figure 28, we can conclude that, when |skew×Rs| <<1, the STAXT power is practically unaffected by the laser phase noise. To further analyse the impact of the phase noise on the power of the ICXT, the instantaneous ICXT power during a given time fraction is analysed.

Figure 29 shows the instantaneous ICXT as a function of the time fraction duration for a laser with 0 Hz and 10 MHz of linewidth. Figure 29 shows that the instantaneous ICXT power is also weakly impaired by the laser phase noise when |skew×Rs| <<1. These results suggest that for the case where |skew×Rs| <<1 the laser linewidth does not impact the STAXT and instantaneous ICXT. Both results shown in figures 28 and 29 are expected. As stated above when we are in the case where |skew×Rs| <<1 and also with |linewidth×skew| <<1, the effects of the laser phase noise on the modulated signal at the interfered core output are negligible.

It is important to mention only the case |linewidth×skew| <<1 is analysed in this subsection. When studying the cases with |skew×Rs| <<1, to get a |linewidth×skew| >>1 a laser with very high linewidth has to be used (i.e. with a skew=1.666 ns, to get a system

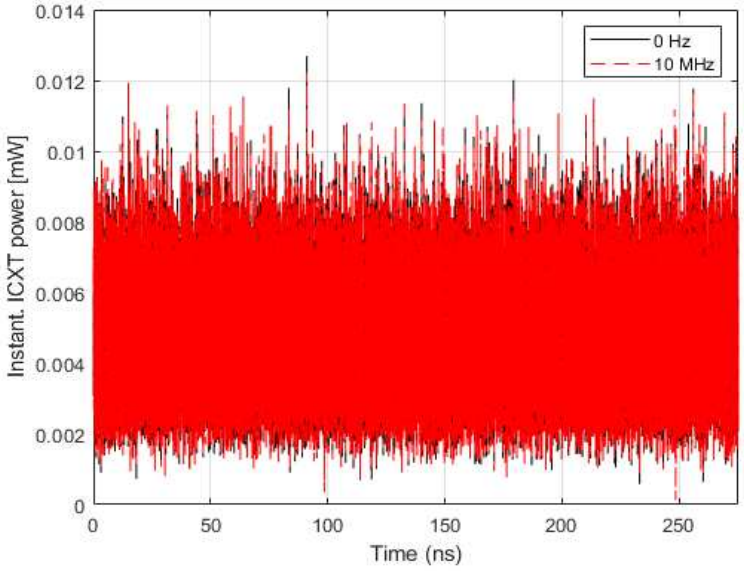

FIGURE 29. Instantaneous ICXT power in function of time when |skew×Rs| <<1 for laser with 0 Hz and 10 MHz of linewidth.

with a |linewidth×skew|=10, a laser with a linewidth of 6 GHz is needed). These lasers have no practical use due to the high phase noise power.

For this reason, in this case the signal will not be decorrelated neither by the symbol rate nor the laser phase noise. As a consequence, in the case with |skew×Rs| <<1 the STAXT is not affected by the laser phase noise of the signal. As stated **??**, for low values of |linewidth×skew| the instantaneous power is not affected by the laser linewidth.

4.4. Effects of the |skew×Rs| on the mean and variance of the STAXT for a system impaired by ICXT and phase noise

In the previous section the impact of the laser phase noise on the STAXT was assessed. In this section we performed an analysis on the impact of the laser linewidths on the STAXT variance.

Figure 30 depicts the mean of the STAXT as a function of the |skew×Rs|. This result sugest that the value of the |skew×Rs| does not have an impact on the STAXT mean. This result was also presented in [**19**]

Figure 31 shows the normalized variance of STAXT as a function of |skew×Rs| for different linewidths. To obtain the normalized variance each case was divided by the maximum variance value (this way the maximum value of the STAXT variance is 1). For all linewidths and each |skew×Rs|, 1000 time fractions were used to obtain the STAXT variance estimation. For all results the symbol rate was fixed at 60 Gbaud/s and only the skew was a variable. These results show that for low |skew×Rs| (i.e. much less than 1) the STAXT variance is independent of the laser linewidth. Furthermore in figure 31 it is shown that there are 2 drops in the STAXT variance. The first drop of 10% in normalized STAXT variance, is around |skew×Rs| = 1, as justified in section 4.2 this is due to multiple symbols affecting the ICXT for higher skews. This drop is independent

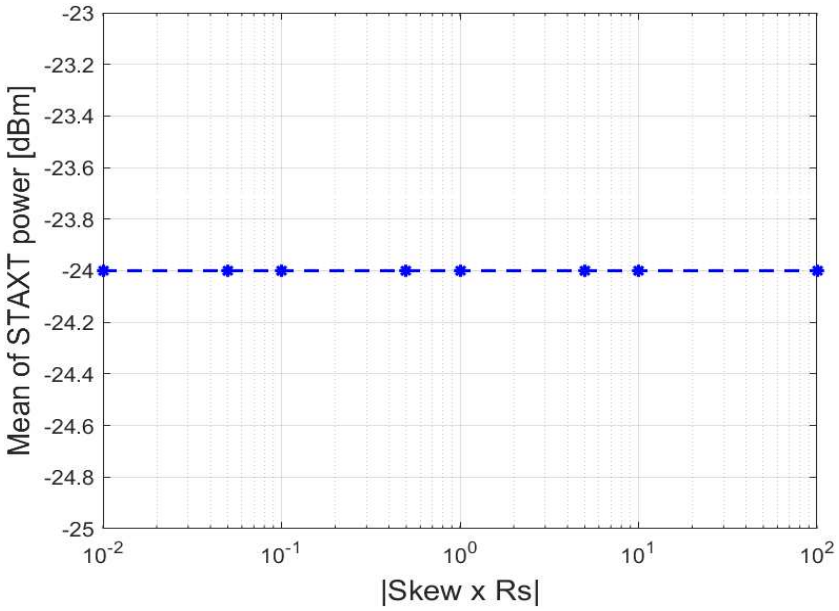

FIGURE 30. Mean STAXT power as a function of |skew×Rs| for different laser linewidths values.

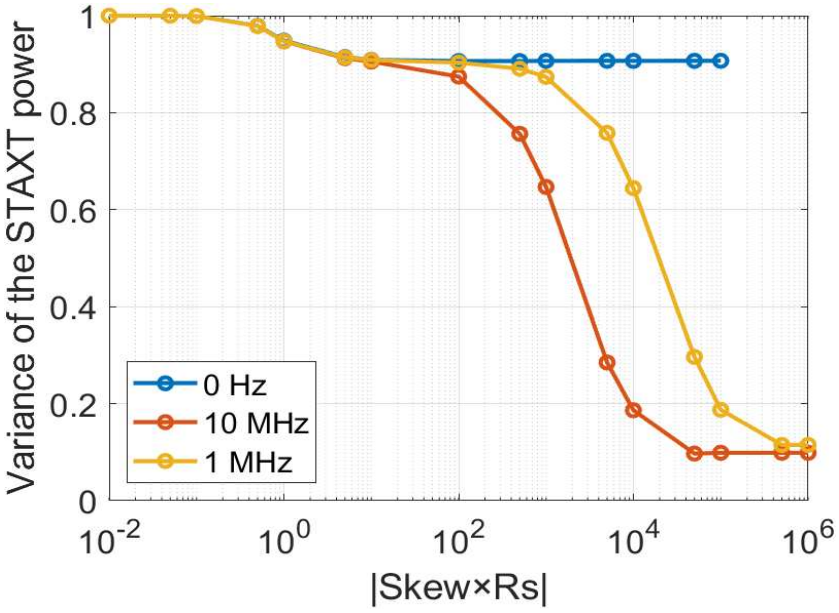

FIGURE 31. Normalized STAXT variance as a function of |skew×Rs| for different laser linewidths values.

from the laser linewidth. The second drop of 80% in normalized STAXT variance, seems to be dependent on the value of the linewidth. For the case with 10 MHz of laser linewidth this drop starts at $|\text{skew}\times\text{Rs}| = 10^2$, for the case with 1 MHz of laser linewidth the drop starts at $|\text{skew}\times\text{Rs}| = 10^3$ and finally, for the ideal case there is no drop in variance. As the point where the drop begins has an order of magnitude difference of 10 (i.e. $\frac{10^3}{10^2} = 10$), and as this is equal to the order of magnitude difference of the laser linewidth ($\frac{10MHz}{1MHz} = 10$), this drop in STAXT variance should be caused by the value of the |linewidth×skew|.

4.5. Effects of the |linewidth×skew| on the STAXT variance and mean

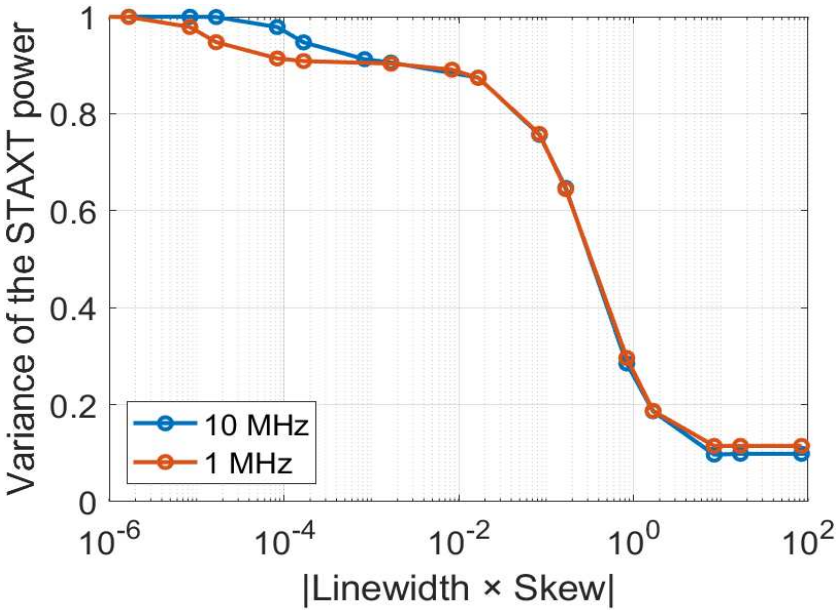

FIGURE 32. Normalized variance as a function of |linewidth×skew| for laser with 10 MHz and 1 MHz of linewidth.

Figure 32 shows the normalized variance of the STAXT for a laser with 10 MHz and 1 MHz as a function of the |linewidth×skew|. Figure 32 was obtained by fixing the linewidth of the laser but varying the skew, this implies that the |skew×Rs| will not be constant in this figure. With figure 32 we can observe that the drop occurs when the |linewidth×skew| approaches 10^2 and it only stabilizes once the value of |linewidth×skew| > 1. This drop can be explained by the value of the instantaneous ICXT in the case where |linewidth×skew| $<<1$ being independent of the phase noise as the skew is lower than time in which all MCF contributions are uncorrelated. This justifies why all lasers behave the same for low |linewidth×skew|. However for |linewidth×skew| >1 there is a dependency on the phase noise, as the different contributions along the MCF are uncorrelated [**35**]. This justifies the difference of 3% of normalized STAXT variance between optical sources present in figure 32.

Figure 33 shows the mean of the STAXT power as a function of the linewidth for different |skew×Rs|. Although there is a greater fluctuation for the case where |skew×Rs| $>>$ 1 of instantaneous ICXT power with increasing linewidth as shown in figure 27 this is not relevant to the final mean. We can conclude with figure 33 that neither the laser linewidth nor the |skew×Rs| between the cores have any impact on the final mean of the STAXT in the system.

Figure 34 shows the variance of the STAXT as a function of the |linewidth×skew| for the case where |skew×Rs| $>>1$, |skew×Rs| $= 1$ and |skew×Rs| $<<1$. This figure was obtained by fixing both the skew and R_s and only varying the linewidth, this way the value of |skew×Rs| stays constant. For low values of |linewidth×skew| all three cases have a small difference in variance. This is to be expected as shown in figure 31 there

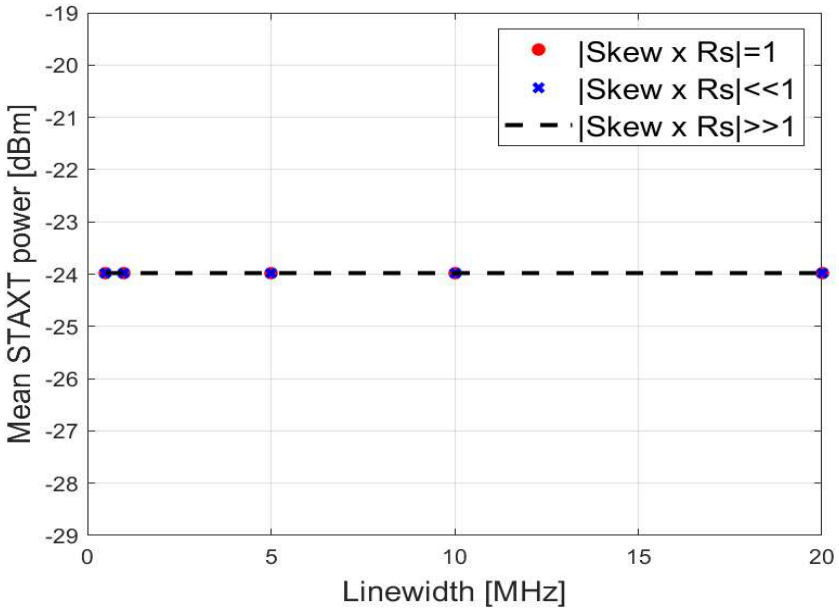

FIGURE 33. Mean of the STAXT power in function of the laser linewidth for different |skew×Rs|.

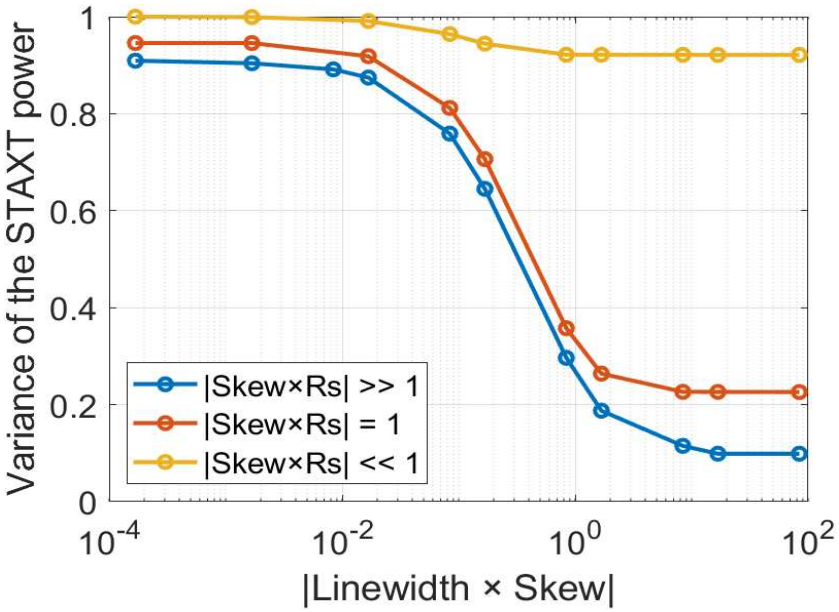

FIGURE 34. Normalized variance of the STAXT power as a function of the product between linewidth and the skew for different values of |skew×Rs|.

is always a difference between each case independent of the linewidth. Furthermore, it is also shown that all 3 cases behave the same, start constant, drop in 10^{-2} until 10^{0} and then becomes constant again, this is for the same reason as 32. This result suggest that the laser linewidth has a higher impact on STAXT variance when |skew×Rs| =1 and |skew×Rs| >>1.

4.6. BER and Outage probability analysis

In this section, we analyse the influence of the ICXT level on the BER and on the outage probability. To assess the BER of the system a Monte Carlo simulation was performed, where the number of errors are counted in every time fraction and when the threshold of 100 errors is reached we estimate the BER using: $\frac{\#errors}{\#bitsent}$, where $\#errors$ is the number of errors, and $\#bitsent$ is the number of bits sent. To calculate the outage probability, the method was described in subsection 3.5.3. Moreover, in the following simulations a |skew×Rs| = 0.01 is used and although the linewidth of the optical source may vary (between 0 Hz and 20 MHz), the |linewidth×skew| will always be much less than 1 for all the cases.

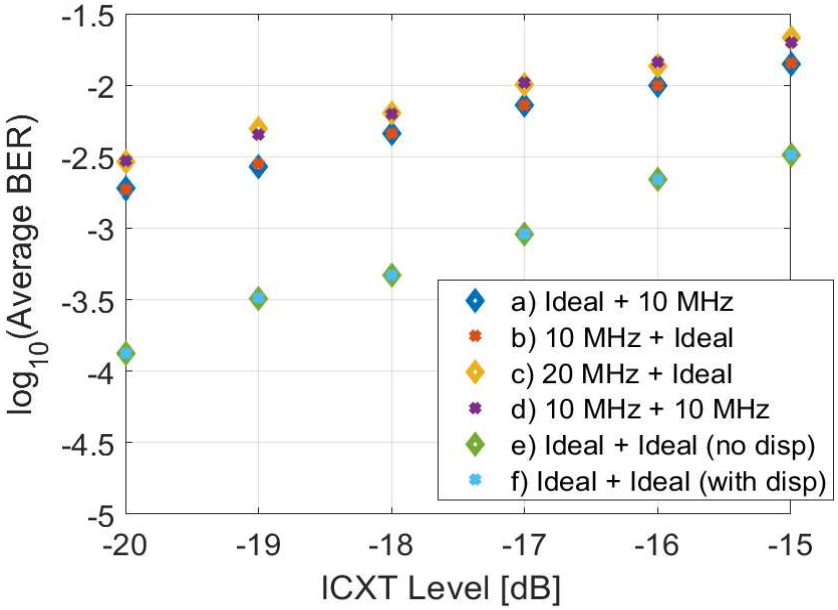

FIGURE 35. Average BER as a function of the ICXT level without considering chromatic dispersion for: a) ideal optical source on the interfered core but interfering core use an optical source with 10 MHz of linewidth, b) ideal optical source on the interfering core but interfered core use an optical source with 10 MHz of linewidth, c) ideal optical source on the interfering core but interfered core use an optical source with 20 MHz of linewidth, d) both cores use an optical source with 10 MHz of linewidth, e) both cores have an ideal optical source but chromatic dispersion is not considered, f) both cores have an ideal optical source and chromatic dispersion is considered.

Figure 35 shows the BER as a function of the ICXT level for a system without any chromatic dispersion. In [**45**] it is shown that the photodetected ICXT depends on the phase noise present in both cores, as the BER has a dependency on the photodetected signal, therefore it was expected that each core optical sources linewidth would have the same impact on the system BER.

Figure 35 shows that for the ideal case (i.e. optical source with 0 Hz of linewidth) the chromatic dispersion has no effect on the BER as the case e) and f) have the same

values for each ICXT level. Furthermore, for the cases a) and b) the figure suggests that the impact of the linewidth on the system BER is not dependent on the core where the higher linewidth optical source is used. Moreover, it is shown with case c) and d) that a core with an optical source with 20 MHz of linewidth has the same BER value as a system with an optical source with 10 MHz in each core. With the exception of case f), these analyses were done without considering chromatic dispersion, however in real cases this is not true.

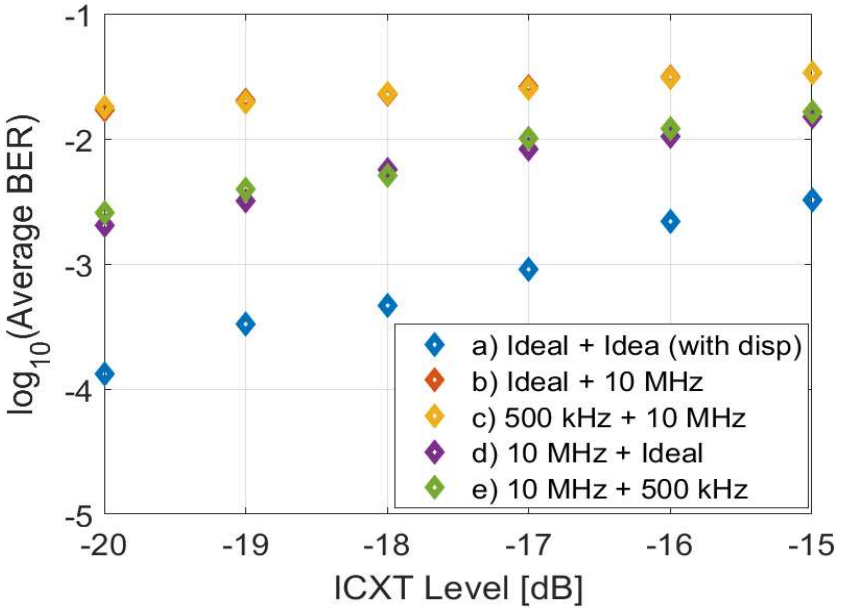

FIGURE 36. BER as a function of the ICXT level for: a) both cores have an ideal optical source, b) ideal optical source for interfering core but interfered core uses an optical source with 10 MHz of linewidth, c) 500 kHz optical source used in the interfering core and interfered core optical source with 10 MHz of linewidth, d) ideal optical source for interfered core but interfering core optical source with 10 MHz of linewidth, e) 500 kHz optical source for interfered core and interfering core optical source with 10 MHz of linewidth.

Figure 36 depicts the average BER as a function of ICXT level considering chromatic dispersion, for the cases where: a) both the interfered and interfering core have an ideal laser (i.e. 0 MHz of linewidth), b) the interfering core has an ideal laser but the interfered core has a laser with 10 MHz linewidth, c) the interfering core has a laser with linewidth of 500 kHz and the interfered core has a laser with 10 MHz linewidth, d) the interfered core has an ideal laser and the interfering core has a laser with linewidth of 10 MHz and e) the interfered core has a laser with 500 kHz of linewidth and the interfering core has a laser with linewidth of 10 MHz. This shows that both lasers will cause some degradation in the system BER, as the case a) has the best performance for all levels of ICXT. However for the cases b) and c) the BER is higher in comparison with cases d) and e). For the cases b) and c) the optical source with 10 MHz is at the interfered core, this implies that the optical source associated with the interfered core has a greater impact on the system BER when considering chromatic dispersion. Since in the interfered core, when

chromatic dispersion is present, the linewidth of the optical source generates phase noise, affecting the system BER by adding a noise effect. For the interfering core, as it is only used to generate the ICXT and we have a |linewidth×skew| much less than 1, the phase noise generated in this core has a low impact on the ICXT field. Furthermore, it can be verified from comparing case a) from figure 35 and case d) from figure 36, that the values of BER are equal in both cases in spite of presence of chromatic dispersion in figure 36. This result shows that the presence of chromatic dispersion only seems to affect the BER when the optical source with an high linewidth is in the interfered core. Moreover, this results show that a DFB laser (in the order of a few MHz) has a much greater impact on the system BER, comparing with the ECL (in the order of kHz). In this case, to obtain a BER level equivalent in both cases, a laser with 10 MHz needs a system with a ICXT level with -5 dB to match the BER on a system employing a laser with 500 kHz. In short, for real systems affected by chromatic dispersion the main source of BER degradation is the optical source on the interfered core, to minimize the BER a lower linewidth laser should be employed in the interfered core.

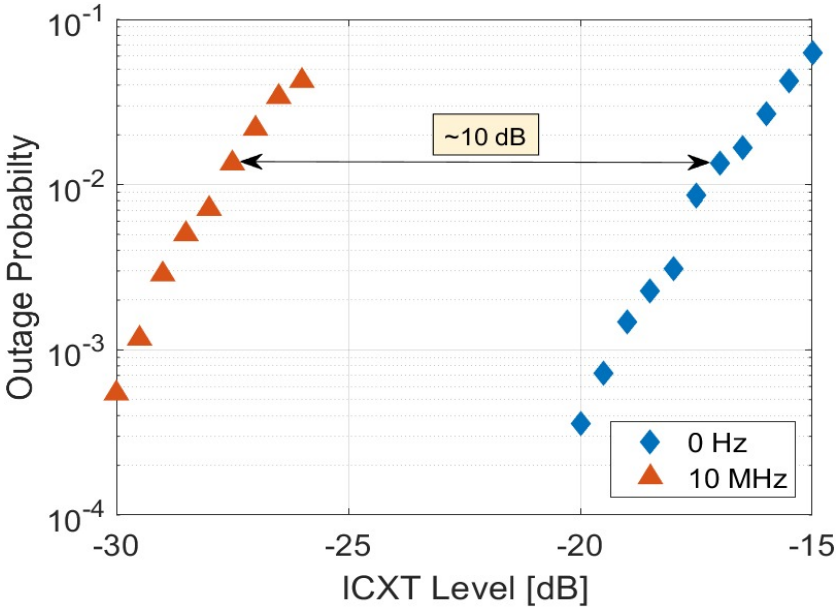

FIGURE 37. Outage probability as a function of the ICXT level when an ideal laser (i.e 0 Hz) or a 10 MHz lasers are employed as optical sources.

Figure 37 compares the outage probability for a system |skew×Rs| <<1 between the ideal case (i.e laser with a linewidth of 0 Hz) and the case where the laser has a linewidth of 10 MHz. This figure suggests that between the outage values for the two cases there is a constant level difference of 10 dB. This is, for a given value of outage probability the difference between the ICXT level for both cases is always about 10 dB. Comparing with [**35**], the margin was 8 dB for a system with |skew×Rs| >>1, which typically has a better performance [**46**].

Chapter 5
Conclusion

5.1. Final conclusion

In this work, a transmission impaired by laser phase noise in a short-reach network employing MCFs and Kramers Kroning receivers was studied. It was assessed the impact of the a laser phase noise on the ICXT and on the system outage probability.

In chapter 2, the revision of literature used for this work was presented. In section 2.1, data centres architectures requirements and problems were presented. In section 2.2, space division multiplexing was described and shown as a possible solution for the problems referred in 2.1. In this section the multicore fiber was also described and introduced as a SDM technology that is used in this work. In section 2.3, the Kramers-Kronig receiver has been introduced as a way of increasing the spectral efficiency of the system at a low cost. Some studies and limitations of this technology has been shown as well. Finally, in section 2.4, the laser phase noise has been described and works employing KK receivers impaired by the phase noise have been shown.

In chapter 3, the system analysed in this work has been characterized. In the following sections different blocks of the system have been analysed. First, at the transmitter, the RRC filter has been described, after the model of DP-MZM modulator has been shown and analysed. After the laser phase noise model used in this work has been characterized. In section 3.3, the MCF model used in this work, the DCM, has been described mathematically and the ICXT model implemented in the simulation has been also validated. In section 3.4, the optical receiver used in this system has been described and validated. Finally, in section 3.5 the metrics used to evaluate the performance of the system have been presented.

In chapter 4, the system proposed in chapter 3 has been evaluated. In section 4.1, the system parameters have been shown and justified. In section 4.2, the impact of the |skew×Rs| on the system without any laser phase noise has been assessed. For this, the STAXT as a function of the number of time fractions, the ICXT instantaneous power as a function of time and the variance of the STAXT power as a function of the |skew×Rs| have been evaluated. In section 4.3, the impact on the STAXT and the ICXT instantaneous power caused by the laser phase noise has been evaluated for systems with |skew×Rs| $>>$ 1 and |skew×Rs| $<<$ 1. In section 4.4, the effects of the |skew×Rs| on the variance of the STAXT in a system impaired by phase noise and ICXT has been assessed. In section 4.5 the effects of the |linewidth×skew| on the STAXT mean and variance has been assessed. Finally, in section 4.6 the BER and outage probability of the system has been analysed. The results present in this section suggest that: (i) systems with |skew×Rs| $<<$1 are dependent on the level of ICXT and the linewidth of the optical source for the interfered

core. (ii) It is also suggested that for a system employing an optical source with high linewidth the main impairment will be the phase noise.

5.2. Future Work

From the conclusion of this work some suggestions for future works are proposed:

- Evaluate the system performance using a digital signal processing equalizer for dispersion compensation
- Evaluate the system performance considering more than one interfering core
- Evaluate the system performance for different types of KK receivers
- Evaluate the impact that optical amplification may cause on the system.

Bibliography

[1] T. Hayashi, T. Nagashima, T. Morishima, Y. Saito, and T. Nakanishi, "Multi-core fibers for data center applications," *IET Conf. Publ.*, vol. 2019, no. CP765, pp. 1–4, 2019.

[2] S. T. Le, K. Schuh, and H. Nguyen Tan, "A closed-form expression for direct detection transmission systems with Kramers-Kronig receiver," *IEEE Photonics Technol. Lett.*, vol. 30, no. 23, pp. 2048–2051, 2018.

[3] W. Marshall, B. Crosignani, and A. Yariv, "Laser phase noise to intensity noise conversion by lowest-order group-velocity dispersion in optical fiber: Exact theory," *Optics letters*, vol. 25, pp. 165–7, 03 2000.

[4] R. J. Essiambre, G. J. Foschini, P. J. Winzer, G. Kramer, and B. Goebel, "Capacity limits of optical fiber networks," *Journal of Lightwave Technology*, vol. 28, no. 4, pp. 662–701, 2010.

[5] J. Krause Perin, A. Shastri, and J. M. Kahn, "Data center links beyond 100 Gbit/s per wavelength," *Opt. Fiber Technol.*, vol. 44, no. April, pp. 69–85, 2018.

[6] Cisco Public, "Cisco global cloud index: forecast and methodology, 2015–2020," pp. 2015–2020, 2016.

[7] K. Saitoh and S. Matsuo, "Multicore fiber technology," *Journal of Lightwave Technology*, vol. 34, no. 1, pp. 55–66, Jan 2016.

[8] A. Mecozzi, "A necessary and sufficient condition for minimum phase and implications for phase retrieval," vol. 13, no. 9, pp. 1–9, 2016.

[9] Y. Kawaguchi and T. Tsuritani, "Ultra-long-haul multicore fiber transmission over 5,000 km using cladding pumped seven-core edfa," in *2017 Opto-Electronics and Communications Conference (OECC) and Photonics Global Conference (PGC)*, 2017, pp. 1–2.

[10] K. Takeshima, T. Tsuritani, Y. Tsuchida, K. Maeda, T. Saito, K. Watanabe, T. Sasa, K. Imamura, R. Sugizaki, K. Igarashi, I. Morita, and M. Suzuki, "51.1-Tbit/s MCF transmission over 2520 km using cladding-pumped seven-core EDFAs," *Journal of Lightwave Technology*, vol. 34, no. 2, pp. 761–767, 2016.

[11] C. Castro, S. Jain, E. D. Man, Y. Jung, J. Hayes, S. Calabrò, K. Pulverer, M. Bohn, S. U. Alam, D. J. Richardson, K. Takenaga, T. Mizuno, Y. Miyamoto, T. Morioka, and W. Rosenkranz, "100-Gb/s transmission over a 2520-km integrated MCF system using cladding-pumped amplifiers," *IEEE Photonics Technol. Lett.*, vol. 29, no. 14, pp. 1187–1190, 2017.

[12] T. Rahman, B. Spinnler, S. Calabrò, E. De Man, K. Pulverer, B. Sommerkorn-Krombholz, C. Castro, T. Mizuno, Y. Miyamoto, K. Takenaga, S. Jain, Y. Jung, S.-u. Alam, and T. Morioka, "108 Tb/s transmission over 120 km of 7-core multicore fiber with integrated cladding pumped multicore amplifiers," in *2018 European Conference on Optical Communication (ECOC)*, 2018, pp. 1–3.

[13] B. Zhu, T. Taunay, M. Fishteyn, X. Liu, S. Chandrasekhar, M. F. Yan, J. M. Fini, E. M. Monberg, and F. V. Dimarcello, "112-Tb/s space-division multiplexed DWDM transmission with 14-b/s/Hz aggregate spectral efficiency over a 76.8-km seven-core fiber," *Opt. Express*, vol. 19, no. 17, pp. 16 665–16 671, Aug 2011.

[14] C. Castro, S. Jain, Y. Jung, E. De Man, S. Calabro, K. Pulverer, M. Bohn, J. R. Hayes, S. U. Alam, D. J. Richardson, Y. Sasaki, T. Mizuno, Y. Miyamoto, T. Morioka, and W. Rosenkranz, "50 ch × 250 Gbit/s 32-QAM transmission over a fully integrated 7-core multicore link," in *2017 European Conference on Optical Communication (ECOC)*, 2017, pp. 1–3.

[15] P. J. Winzer, D. T. Neilson, and A. R. Chraplyvy, "Fiber-optic transmission and networking: the previous 20 and the next 20 years invited," *Opt. Express*, vol. 26, no. 18, pp. 24 190–24 239, Sep 2018.

[16] I. Ashry, Y. Mao, A. Trichili, B. Wang, T. K. Ng, M.-S. Alouini, and B. S. Ooi, "A review of using few-mode fibers for optical sensing," *IEEE Access*, vol. 8, pp. 179 592–179 605, 2020.

[17] J. Sakaguchi, Y. Awaji, N. Wada, A. Kanno, T. Kawanishi, T. Hayashi, T. Taru, T. Kobayashi, and M. Watanabe, "109-Tb/s (7×97×172-Gb/s SDM/WDM/PDM) QPSK transmission through 16.8-km homogeneous multi-core fiber," in *Optical Fiber Communication Conference/National Fiber Optic Engineers Conference 2011*. Optica Publishing Group, 2011, p. PDPB6.

[18] D. Soma, Y. Wakayama, S. Beppu, S. Sumita, T. Tsuritani, T. Hayashi, T. Nagashima, M. Suzuki, H. Takahashi, K. Igarashi, I. Morita, and M. Suzuki, "10.16 peta-bit/s dense SDM/WDM transmission over low-DMD 6-mode 19-core fibre across C+L band," in *2017 European Conference on Optical Communication (ECOC)*, 2017, pp. 1–3.

[19] B. R. P. Pinheiro, J. L. Rebola, and A. V. T. Cartaxo, "Analysis of inter-core crosstalk in weakly-coupled multi-core fiber coherent systems," *Journal of Lightwave Technology*, vol. 39, no. 1, pp. 42–54, 2021.

[20] D. L. Butler, M.-J. Li, B. J. Hoover, V. N. Nazarov, D. D. Fortusini, J. P. Luther, Y. Geng, and R. R. Grzybowski, "Multicore optical fiber and connectors for short reach, high density links," in *IEEE Photonics Conference 2012*, 2012, pp. 878–879.

[21] A. V. T. Cartaxo, T. M. F. Alves, B. J. Puttnam, R. S. Luís, Y. Awaji, and N. Wada, "DD-OFDM multicore fiber systems impaired by intercore crosstalk and laser phase noise," in *2017 19th International Conference on Transparent Optical Networks (ICTON)*, 2017, pp. 1–5.

[22] J. L. Rebola, T. M. F. Alves, and A. V. T. Cartaxo, "Outage probability due to intercore crosstalk from multiple cores in short-reach networks," *IEEE Photonics Technology Letters*, vol. 33, no. 6, pp. 281–284, 2021.

[23] Z. Li, M. S. Erkılınç, K. Shi, E. Sillekens, L. Galdino, B. C. Thomsen, P. Bayvel, and R. I. Killey, "SSBI mitigation and the Kramers–Kronig scheme in single-sideband direct-detection transmission with receiver-based electronic dispersion compensation," *Journal of Lightwave Technology*, vol. 35, no. 10, pp. 1887–1893, 2017.

[24] S. T. Le, K. Schuh, M. Chagnon, F. Buchali, R. Dischler, V. Aref, H. Buelow, and K. M. Engenhardt, "1.72-tb/s virtual-carrier-assisted direct-detection transmission over 200 km," *Journal of Lightwave Technology*, vol. 36, no. 6, pp. 1347–1353, Mar 2018.

[25] X. Chen, C. Antonelli, S. Chandrasekhar, G. Raybon, A. Mecozzi, M. Shtaif, and P. Winzer, "Kramers–Kronig receivers for 100-km datacenter interconnects," *Journal of Lightwave Technology*, vol. 36, no. 1, pp. 79–89, 2018.

[26] X. Chen, C. Antonelli, S. Chandrasekhar, G. Raybon, J. Sinsky, A. Mecozzi, M. Shtaif, and P. Winzer, "218-Gb/s single-wavelength, single-polarization, single-photodiode transmission over 125-km of standard singlemode fiber using Kramers-Kronig detection," pp. 1–3, 2017.

[27] C. Sun, D. Che, H. Ji, and W. Shieh, "Study of chromatic dispersion impacts on Kramers–Kronig and SSBI iterative cancellation receiver," *IEEE Photonics Technology Letters*, vol. 31, no. 4, pp. 303–306, 2019.

[28] D. Kong, E. P. da Silva, Y. Sasaki, K. Aikawa, F. Da Ros, M. Galili, T. Morioka, H. Hu, and L. K. Oxenløewe, "909.5 Tbit/s dense SDM and WDM transmission based on a single source optical frequency comb and Kramers-Kronig detection," *IEEE Journal of Selected Topics in Quantum Electronics*, vol. 27, no. 2, pp. 1–8, 2021.

[29] I. Tavakkolnia, C. Chen, H. Haas, and Y. Tan, "Terabit optical wireless-fiber communication with Kramers-Kronig receiver—part I," *IEEE Communications Letters*, vol. 26, no. 9, pp. 1964–1968, 2022.

[30] I. Tavakkolnia, C. Chen, Y. Tan, and H. Haas, "Terabit optical wireless-fiber communication with Kramers-Kronig receiver—part II," *IEEE Communications Letters*, vol. 26, no. 9, pp. 1969–1973, 2022.

[31] C. Antonelli, A. Mecozzi, and M. Shtaif, "Kramers Kronig PAM transceiver and two-sided polarization-multiplexed Kramers Kronig transceiver," *arXiv*, vol. 36, no. 2, pp. 468–475, 2017.

[32] C. Antonelli, M. Shtaif, and A. Mecozzi, "Kramers-Kronig PAM transceiver," pp. 1–3, 2017.

[33] A. Cartaxo, *Transmissão por Fibra Óptica*, 2005.

[34] K. Schuh and S. T. Le, "180 Gb/s 64QAM transmission over 480 km using a DFB laser and a Kramers-Kronig receiver," in *2018 European Conference on Optical Communication (ECOC)*, 2018, pp. 1–3.

[35] T. M. F. Alves, A. V. T. Cartaxo, and J. L. Rebola, "DD-OOK multicore fiber systems impaired by intercore crosstalk and laser phase noise," *Journal of Lightwave Technology*, vol. 40, no. 5, pp. 1544–1551, 2022.

[36] M. Azizoglu and P. Humblet, "Optical DPSK with generalized phase noise model and narrowband reception," in *Proceedings of ICC '93 - IEEE International Conference on Communications*, vol. 3, 1993, pp. 1591–1596 vol.3.

[37] S. Ishimura, Y. Nakano, and T. Tanemura, "Impact of laser phase noise on self-coherent transceivers employing high-order QAM formats," *Journal of Lightwave Technology*, vol. 39, no. 19, pp. 6150–6158, 2021.

[38] A. V. T. Cartaxo and T. M. F. Alves, "Discrete changes model of inter-core crosstalk of real homogeneous multi-core fibers," *Journal of Lightwave Technology*, vol. 35, no. 12, pp. 2398–2408, 2017.

[39] R. O. Soeiro, T. M. Alves, and A. V. Cartaxo, "Dual polarization discrete changes model of intercore crosstalk in multi-core fibers," *IEEE Photonics Technol. Lett.*, vol. 29, no. 16, pp. 1395–1398, 2017.

[40] T. M. F. Alves and A. V. T. Cartaxo, "Intercore crosstalk in homogeneous multicore fibers: Theoretical characterization of stochastic time evolution," *Journal of Lightwave Technology*, vol. 35, no. 21, pp. 4613–4623, 2017.

[41] T. M. F. Alves and A. Cartaxo, "Characterization of the stochastic time evolution of short-term average intercore crosstalk in multicore fibers with multiple interfering cores," *Opt. Express*, vol. 26, no. 4, pp. 4605–4620, Feb 2018.

[42] A. Mecozzi, C. Antonelli, and M. Shtaif, "Kramers–kronig coherent receiver," *Optica*, vol. 3, no. 11, pp. 1220–1227, Nov 2016. [Online]. Available: https://opg.optica.org/optica/abstract.cfm?URI=optica-3-11-1220

[43] A. Cartaxo and T. Alves, "Theoretical and experimental performance evaluation methods for dd-ofdm systems with optical amplification," *Journal of Microwaves, Optoelectronics and Electromagnetic Applications*, vol. 10, pp. 82–94, 06 2011.

[44] G. Rademacher, R. S. Luís, B. J. Puttnam, Y. Awaji, and N. Wada, "Crosstalk dynamics in multicore fibers," *Opt. Express*, vol. 25, no. 10, pp. 12 020–12 028, May 2017.

[45] T. M. F. Alves, A. V. T. Cartaxo, R. S. Luís, B. J. Puttnam, Y. Awaji, and N. Wada, "Intercore crosstalk in direct-detection homogeneous multicore fiber systems impaired by laser phase noise," *Opt. Express*, vol. 25, no. 23, pp. 29 417–29 431, Nov 2017. [Online]. Available: https://opg.optica.org/oe/abstract.cfm?URI=oe-25-23-29417

[46] T. M. Alves, A. V. Cartaxo, and J. L. Rebola, "Stochastic properties and outage in crosstalk-impaired ook-dd weakly-coupled mcf applications with low and high skew×bit-rate," *IEEE J. Sel. Top. Quantum Electron.*, vol. 26, no. 4, 2020.

Appendix A
Electrical noise

When detected by a PIN, the photo-current signal is weak, so the receiver includes an electrical pre-amplifier at the photo-diode output [**33**]. Furthermore the PIN also generates some thermal noise due to the load present in the circuit.

The electrical noise present in the PIN can be characterized by the receiver noise equivalent power (NEP) [**33**]. With the NEP is possible to get the two sided PSD of the electrical circuit noise, the following equation is used:

$$S_c(f) = (NEP * R_\lambda)^2 \tag{A.1}$$

Where R_λ is the PIN responsivity. Using the two sided PSD of the electrical circuit noise, the noise power can be calculated using the equation A.2:

$$p_n = S_c \times f_s \tag{A.2}$$

Where f_s is the sampling frequency of the simulation. Finally, to generate the noise in the simulation a noise array with a normal distribution is created. Afterwards, it is induce the noise power calculated using equation A.2 to generate the final noise array that is added to the signal.